Phase response analyses support a relaxation oscillator model of locomotor rhythm generation in *Caenorhabditis elegans*

Hongfei Ji[1,*], Anthony D. Fouad[1,*], Shelly Teng[1], Alice Liu[1], Pilar Alvarez-Illera[1], Bowen Yao[1], Zihao Li[1], and Christopher Fang-Yen[1,2]

[1]Department of Bioengineering, School of Engineering and Applied Science, University of Pennsylvania, Philadelphia, PA 19104.
[2]Department of Neuroscience, Perelman School of Medicine, University of Pennsylvania, Philadelphia, PA 19104.

*Equal contributions

Correspondence: fangyen@seas.upenn.edu

Abstract

Neural circuits work together with muscles and sensory feedback to generate motor behaviors appropriate to an animal's environment. In *C. elegans,* forward locomotion consists of dorsoventral undulations that propagate from anterior to posterior. How the worm's motor circuit generates these undulations and modulates them based on external loading is largely unclear. To address this question, we performed quantitative behavioral analysis of *C. elegans* during free movement and during transient optogenetic muscle inhibition. Undulatory movements in the head were found to be highly asymmetric, with bending toward the ventral or dorsal directions occurring slower than straightening toward a straight posture during the locomotory cycle. Phase shifts induced by brief optogenetic inhibition of head muscles showed a sawtooth-shaped dependence on phase of inhibition. We developed a computational model based on proprioceptive postural thresholds that switch the active moment of body wall muscles. We show that our model, a type of relaxation oscillator, is in quantitative agreement with data from free movement, phase responses, and previous results for frequency and amplitude dependence on the viscosity of the external medium. Our results suggest a neuromuscular mechanism that enables *C. elegans* to coordinate rhythmic motor patterns within a compact circuit.

Introduction

Animal locomotion represents a complex interplay between neural activity, muscle contractions and relaxations, sensory feedback, and biomechanical interactions with the animal's body and the external environment (Fig. 1A; 1–3). Patterned motor signals typically originate from central pattern generators (CPGs), neuronal circuits capable of generating rhythmic patterns in the absence of rhythmic inputs, including rhythmic feedback from sensory systems (4–10). Sensory feedback, however, plays a critical role in coordinating and modulating these rhythms in the intact animal (2, 11–14).

Sensory feedback mechanisms allow animals to adapt locomotory patterns to their surroundings (15, 16) as well as counteract unexpected perturbations (17). In leeches (18, 19) and *Drosophila* (20, 21), specialized proprioceptive neurons and sensory receptors in body muscles detect sensory inputs to regulate and coordinate the centrally generated motor patterns. Similarly, in limbed vertebrates, proprioceptors located in muscles, joints, and/or skin detect body movements and interact with premotor interneurons to coordinate limb movements (13). Furthermore, sensory inputs induced by direct electronic stimulation to receptor cells (22) or by forceful movements of body segments (23) can also entrain the CPG to imposed patterns.

The nematode *Caenorhabditis elegans*, with its well-mapped nervous system (24, 25), genetic manipulability (26–28), and optical transparency, represents a unique model for obtaining an integrative

understanding of the mechanisms of locomotory rhythm generation and sensory feedback modulation.

C. elegans forward locomotion consists of anterior-to-posterior dorsoventral undulations (29). These movements are mediated by a neuromuscular circuit consisting of interneurons, excitatory cholinergic motor neurons, inhibitory GABAergic motor neurons, and body wall muscles. Laser ablation studies have shown that the cholinergic B-type motor neurons are required for forward locomotion (30). The GABAergic D-type motor neurons provide dorsoventral cross-inhibition to the body wall muscles and are essential for maintaining normal wave shape and frequency during forward locomotion (31, 32). A set of premotor interneurons (AVB, PVC, AVA, AVD, and AVE) regulate directions of *C. elegans* movement (33–35). Ablation of all premotor interneurons or the D-type motor neurons does not deprive *C. elegans* of the ability to move forward (30, 36, 37), suggesting that a network consisting of excitatory motor neurons and/or muscles may be sufficient to generate the rhythmicity. Optogenetic and lesion experiments have shown that multiple oscillators exist in the ventral nerve cord (38). However, specific mechanism and the corresponding constituents that give rise to these oscillators have not been addressed.

In *C. elegans*, proprioceptive feedback is crucial for modulating rhythmic motor behavior. Experimental studies have identified several neuron classes that are involved in proprioception to mediate the rhythmic patterns in worms. The B-type motor neurons have been shown to mediate proprioceptive coupling between anterior to posterior bending during forward locomotion (11). The SMDD motor neurons, localized at the head, have been identified as proprioceptive neurons to regulate head steering during locomotion (39). Both the B-type motor neurons and the SMDD head motor neurons have long asynaptic processes along the body that have been hypothesized to have proprioceptive function (24) and have been suggested as candidate locomotor CPG elements (40). In addition, two types of neurons, the DVA and PVD interneurons, have also been described as having proprioceptive roles in the regulation of worm's body bend movement. The cell DVA has been shown to exhibit proprioceptive properties with a dependence on a mechanosensitive channel, TRP-4, which acts as a stretch receptor to regulate the body bend amplitude during locomotion (41). In the case of PVD, a recent study (42) has revealed that body stretches induce local dendritic calcium transients in PVD and dendritic release of a neuropeptide NLP-12 which appears to regulate the amplitude of sinusoidal body movements. However, whether these proprioceptive feedback systems contribute to locomotory rhythm generation remains unknown.

A systems-level understanding of *C. elegans* locomotion requires consideration of neural, muscular, and mechanical degrees of freedom. Such analyses are often tractable only by computational modeling methods. Computational models for motor behavior have long been an important complement for experimental approaches. An early model of *C. elegans* locomotion (43) assumes that a CPG located in the head initiates dorsoventral bends and that a combination of neuronal and sensory feedback mechanisms propagates the waves in the posteriorward direction. In this model, sensory feedback plays a modulatory role in producing smoother curvature waves but is not mandatory for rhythm generation itself.

Other computational models have aimed to describe how the motor circuit generates rhythmicity. Karbowski *et al*. (44) reported a detailed neural model for the forward-moving circuit, including treatments of all major neural components and connectivity. This model included a CPG in the head responsible for generating oscillations. Specifically, oscillatory rhythm in the head arises from the effective cross-inhibition between the ventral and dorsal groups of interneurons. In contrast, Bryden and Cohen (45) developed a neural model in which each segment along the body is capable of generating oscillations. In this model, a circuit of AVB interneurons and B-type motor neurons suffices to generate robust locomotory rhythms that resemble experimental observations even without cross-inhibition.

Other models have examined how *C. elegans* adapts its undulatory wavelength, frequency, and amplitude as a gait adaptation to external load (46, 47). To account for these changes, Boyle *et al.* (48) combined the motor circuit model of Bryden and Cohen with additional assumptions of stretch sensitivity and bistability in motor neurons, and worm body biomechanical constraints, to create a model that reproduced the changes in undulatory wave patterns under a range of external conditions.

A key goal of any model is to make testable predictions that can provide guidance for experiments. Predictive power is generally greater when a model uses a relatively small set of free parameters (49). Previous detailed models of *C. elegans* locomotion have a large number of free parameters (up to 40 for each

oscillator segment (44, 48)) and rely on assumptions about neural dynamics and synaptic function that are not directly supported by experimental evidence. At the same time, the set of experimental observations used to test models has been relatively modest in terms of the strengths of constraints. The complexity of computational models and a paucity of experimental constraints in *C. elegans* locomotion has represented a limitation to a systems-level, quantitative understanding of motor rhythm generation.

In this work, we sought to develop a phenomenological model to describe an overall mechanism of rhythm generation but not the detailed dynamics of specific circuit elements. We aimed to incorporate biomechanical constraints of the worm's body and its environment (47, 50, 51), as well as account for how sensory feedback is incorporated. To improve predictive power, we aimed to minimize the number of free parameters used in the model. Finally, we sought to optimize and test this model with new experiments as well as with published findings.

To experimentally probe mechanisms of rhythmic motor generation, we measured the phase response curve (PRC) upon transient optogenetic inhibition of the head muscles. We found that the worms displayed a biphasic, sawtooth-shaped PRC with sharp transitions from phase delay to advance. Based on this finding, we developed a computational model of rhythm generation in the *C. elegans* motor circuit in which a relaxation-oscillation process underlies the worm's rhythmic dorsal-ventral alternation.

Our model reproduces the observed PRC and also describes the locomotory dynamics around optogenetic inhibitions in a manner that closely fit our experimental observations. Our model also agrees with quantitative results on gait adaptation to external load and the intrinsic asymmetry in time-dependent curvature patterns of undulating worms. Our model contains only 5 free parameters but reproduces several key features of locomotion including some that have not been previously reported.

Our experimental findings and computational model together yield insights into how *C. elegans* generates rhythmic locomotion.

Results

Phase Portrait Analysis reveals Nonsinusoidal Dynamics in *C. elegans* Free Locomotion

To gain insight into wave generation, we first sought to examine in detail the quantitative behavioral characteristics of worms during uninterrupted forward locomotion.

To quantify the undulatory dynamics of body bending, we computed the time-varying curvature along the centerline of the body (11, 47, 52, 53) from analysis of dark field image sequences of worms during forward locomotion. In order to quantitatively treat the drag between the body and its environment, we examined locomotion of worms swimming in dextran solutions which exhibit Newtonian flow characteristics (see *SI;* 49). The normalized body coordinate is defined by fraction of distance from head to tail (Fig. 2A). The curvature κ at each point along the centerline of the body is the reciprocal of local radius of curvature ($\kappa = 1/R$, Fig. 2A). Here we represent body curvature using the dimensionless variable $K = \kappa \cdot L$, where L is the length of the worm. We focus on curvature dynamics of worm's head region (0.1-0.3 body coordinate, Fig. 2B) where a positive curvature represents ventral bending and a negative one represents dorsal bending.

To examine the characteristics of the worm's motor rhythm generator, we generated phase portraits, a geometric representation of a dynamical system's trajectories over time (54), in which the time derivative of the curvature is plotted against the curvature itself. If the curvature were sinusoidal over time, as it is often modeled in slender swimmers (43, 47, 55, 56), the time derivative of curvature would also be sinusoidal, with a phase shift of $\pi/4$ (in radians) relative to the curvature, and the resulting phase portrait would be symmetric about both the K and dK/dt axes.

From the recordings of free locomotion of worms, we found that the curvature phase trajectory is in fact non-ellipsoidal and strongly asymmetric with respect to reflection across the K or dK/dt axes (Fig. 2 C,D).

Plots of both the phase portrait (Fig. 2D) and the time dependence (Fig. 2C) show that K and dK/dt are far from sinusoidal. The nature of the nonsinusoidal dynamics will be explored further below.

Transient Optogenetic Inhibition of Head Muscles Yields a Slowly Rising, Rapidly Falling Phase Response Curve

To explore the intrinsic structure of the *C. elegans* motor rhythm generation system, we performed a phase response analysis of the worm's locomotion upon transient optogenetic inhibitions. The phase response curve (PRC) describes the change in phase of an oscillation induced by a perturbation as a function of the phase at which the perturbation is applied, and is often used to characterize biological and nonbiological oscillators (54, 57, 58).

We used a closed-loop system for targeting specific parts of the worm (38, 53) to apply brief pulses of 532 nm laser illumination to the heads of worms expressing the inhibitory opsin *NpHR* in body wall muscles (Supplemental Video 1). Simultaneous muscle inhibition on both the ventral and dorsal sides causes *C. elegans* to straighten due to its internal elastic forces (47). Brief (0.1 s duration) inhibition of the head muscles during forward locomotion was followed by a maximum paralysis approximately 0.3 s after the end of the pulse, then a resumption of normal undulation roughly 0.5 s after the end of the pulse (Fig. 3 A,B).

Using data from 991 illuminations in 337 worms, we analyzed the animals' recovery from transient paralysis as a function of the phase at which the illumination occurred. We define phase as in Fig. 3D, such that $\phi = 0$ at the point of maximum ventral bending. When inhibition occurred with phase in the interval $[0, \pi/6]$, the head typically straightened briefly and then continued the previous bend, resulting in a phase delay for the oscillation (Fig. 3 C-E). When inhibition occurred with phase in the interval $[\pi/3, \pi/2]$, the head usually appeared to discontinue the previous bend movement, which resulted in a small phase advance (Fig. 3 F-H). When inhibition occurred with phase in the interval $[2\pi/3, 5\pi/6]$, the head response was similar to that between the interval $[0, \pi/6]$, and also resulted in a phase delay (Fig. 3 I-K).

Combining the data from all phases of inhibition yielded a sawtooth-shaped PRC (Fig. 3 L,M) with two sharp transitions from phase delay to advance as well as two relatively slow ascending transitions from phase advance to delay. In control worms, which do not express *NpHR* in the body wall muscles (see *Methods*), the resulting PRC curve shows no significant phase shift over all phases of illumination (Fig. S1).

We asked whether the sharp downward transitions in the PRC represent a continuous decrease or instead result from averaging data from a bimodal distribution. When we plotted the distribution of the same data in a 2-D representation (Fig. 3M) we found that the phase shifts display a piecewise, linear increasing dependence on the phase of inhibition with two abrupt jumps occurring at $\phi \approx \pi/3$ and $4\pi/3$, respectively. This result shows that the sharp decreasing transitions in PRC reflect bimodality in the data rather than continuous transitions.

Sawtooth-shaped PRCs are observed in a number of systems with oscillatory dynamics, including the van der Pol oscillator (59), and may reflect a phase resetting property of an oscillator with respect to a perturbation (54, 57). Further interpretation of the PRC results is given below.

Worm Muscles Display a Rapid Switch-like Alternation during Locomotion

As a first step in interpreting and modeling our findings, we estimated the patterns of muscle activity in freely moving worms, in part by drawing on previous biomechanical analyses of nematode movement (47, 50, 51).

In mechanics, a moment is a measure of the ability of forces to produce twisting about an axis. Body wall muscles create local dorsal or ventral bending by generating active moments acting on an axis extending from the dorsal to ventral sides of the body. In addition to the active moments from muscles, there are also passive moments generated by the worm's internal elasticity and by the forces due to the interaction of the worm with its external environment.

We estimated the output patterns of the active muscle moment that drives the head oscillations of freely moving worms immersed in viscous solutions. Following previous analyses of *C. elegans* locomotor biomechanics under similar external conditions (47), the scaled active muscle moment can be described as a linear combination of the curvature and the time derivative of the curvature (Eq. 1; also see *Methods* and *SI*). We observed that in the phase portrait graph (Fig. 2D), there are two nearly linear portions of the curve. We

hypothesized that these linear portions correspond to two bouts during which the active muscle moment is nearly constant.

Using fits to the phase plot trajectory (see *Methods* and *SI*) we estimated the waveform of the active muscle moment as a function of time (Fig. 2D *Inset*). We found that the net active muscle moment alternates between two plateau portions during forward locomotion. From the slope of the steep portions on this curve, we estimated the time constant for transitions between active moments to be $\tau_m \approx 50\ ms$. This time constant is an order of magnitude smaller than the duration of each muscle plateau period ($\approx\ 0.5\ s$), suggesting that the system undergoes rapid switches of muscle contractions between two saturation states.

A Relaxation Oscillator Model Explains Nonsinusoidal Dynamics

We reasoned that the rapid transitions of the active muscle moment might reflect a switching mechanism in the locomotory rhythm generation system. We hypothesized that the motor system generates locomotory rhythms by switching the active moment of the muscles based on proprioceptive thresholds.

To elaborate these ideas further, we developed a quantitative model of locomotory rhythm generation. We consider the worm as a viscoelastic rod where the scaled curvature *K(t)* varies according to:

$$K(t) + \tau_u \frac{dK(t)}{dt} = M_a(t), \qquad [\mathbf{1}]$$

where τ_u describes the time scale of bending relaxation and $M_a(t)$ is the time-varying active muscle moment scaled by the bending modulus and the body length (see detailed derivations in *SI*). We note that in a stationary state ($dK/dt = 0$), the curvature would be equal to the scaled active muscle moment. That is, the scaled active moment represents the static curvature that would result from a constant muscle moment.

We define a proprioceptive feedback variable P as a linear combination of the current curvature value and the rate of change of curvature. In our model, once this variable reaches either of two thresholds P_{th} and $-P_{th}$ (Fig. 4D), the active muscle moment undergoes a change of sign (Fig. 4E), causing the head to bend toward the opposite direction (Fig. 4B).

Our model has 5 parameters: (1) τ_u, the bending relaxation time scale, (2) τ_m, the muscle switching time scale, (3) M_0, the amplitude of the scaled active muscle moment, (4-5) b and P_{th}, which determine the switch threshold. The first 3 parameters were directly estimated from our experimental results from freely moving worms (see *SI*). Parameters b and P_{th} were obtained by fitting the model to the experimental phase response curve, which is described in the following section (also see *SI*).

With this set of parameters, we calculated the model dynamics as represented by phase portrait (Fig. 4C) as well as curvature waveform in one cycle period (Fig. 4F). We found that in both cases the model result agreed with our experimental observations. Our model captures the asymmetric phase portrait trajectory shape found from our experiments (Fig. 2D). Our model describes the asymmetry of head bending during locomotion: bending toward the ventral or dorsal directions occurs slower than straightening toward a straight posture during the locomotory cycle (Fig. 4F *Inset*).

Considering the hypothesized mechanism under the biomechanical background (Eq. 1), our model provides a simple explanation for the observed bending asymmetry during locomotion. According to our model, the active muscle moment is nearly constant during each period between transitions of the muscle moment. Biomechanical analysis under this condition predicts an approximately exponential decay in curvature, which gives rise to an asymmetric feature during each half period (Fig. 4F).

The Model Reproduces Responses to Transient Optogenetic Inhibition

We performed simulations of optogenetic inhibitions in our model. To model the transient muscle paralysis, the muscle moment is modulated by a bell-shaped function of time (Fig. S5; also see *SI*) such that, upon inhibition, it decays toward zero and then recovers to its normal value, consistent with our behavioral observations (Fig. 3B).

From simulations with different sets of model parameters, we found that the model PRCs consistently shared the sawtooth shape previously found in experiments, though differing in height and timing of the phase resetting transitions. Besides the model parameters τ_u, M_0, and τ_m that had been explicitly estimated from free-moving experiments, we performed a global optimization procedure (see *SI*) to determine the other

parameters (including b, P_{th}, and parameters for describing the optogenetically induced muscle inhibitions) to best fit the experimental PRC with a minimum mean squared error (MSE) (Fig. 5A). For the parameters b and P_{th}, the optimization estimated their values to be $b = 0.046\ s$ and $P_{th} = 2.33$, as shown on the phase portraits (grey dashed lines in Figs. 4C, 5B and 5D).

The threshold-switch mechanism model provides an explanation for the observed sawtooth-shaped PRC. By comparing model phase portrait graphs around inhibitions occurring at different phases (Fig. 5 B-E), we found that the consequent phase shift depends on the relative position of the inhibition with respect to the switch points on the phase plane: (1) if the effect of the inhibition occurs before the system reaches its switch point (Fig. 5B), the system will recover by continuing the previous bend and the next switch in the muscle moment will be postponed, thereby leading to a phase delay (Fig. 5C); (2) as the inhibition progressively approaches the switch point, one would expect that the next switch in the muscle moment will also be progressively postponed; this explains the increasing portions of the PRC; (3) if the inhibition coincides with the switch point (Fig. 5D), the muscle moment will be switched at this point and the system will recover by aborting the previous bend tendency, resulting in a small phase advance (Fig. 5E); this explains the two sharp downward transitions in the PRC.

The Model Predicts Phase Response Curves for Single-Side Muscle Inhibition

As a further test of the model, we asked what PRCs would be produced with only the ventral or dorsal head muscles being transiently inhibited. In the model, the muscle activity is represented using the scaled active moment of muscles. We conducted model simulations (see *SI*) to predict the PRCs for transient inhibitions of muscles on the dorsal side (Fig. 6A, *Upper*) and ventral side (Fig. 6B, *Upper*), respectively.

To experimentally perform phase response analysis of single-side muscle inhibitions, we visually distinguished each worm's dorsoventral orientation (via vulva location) and targeted light to a specific side of the animal. Transiently illuminating (0.1 s duration) dorsal or ventral muscles in the head region of the transgenic worms (Muscle::*NpHR*) induced a brief paralyzing effect when the segment was bending toward the illuminated side, but did not induce a significant paralyzing effect when the segment was bending away from the illuminated side (Fig. S6).

Combining the experimental data from all phases of dorsal-side or ventral-side inhibition yielded the corresponding PRCs (Fig. 6 A,B, respectively), from which we found that both PRCs show a peak in the phase range during which the bending side is illuminated but shows no significant phase shift in the other phase range. The experimental observations are qualitatively consistent with model predictions.

We found that the PRC of dorsal-side illumination shows a smaller paralytic response than that of ventral-side illumination. This discrepancy may be due to different degrees of paralysis achieved during ventral vs. dorsal illumination (Fig. S6), possibly due to differences in levels of opsin expression and/or membrane localization. We therefore modulated the parameter for describing degree of paralysis when simulating the PRC of the dorsal-side illumination to qualitatively account for this discrepancy (*SI*).

The Model is Consistent with the Dependence of Wave Amplitude and Frequency on External Load

C. elegans can swim in water and crawl on agar gel surface, exhibiting different undulatory gaits characterized by different frequencies, amplitudes, and wavelengths (Fig. 7A). Previous studies (46, 47) have shown that increasing viscosity of external environments induces a continuous transition from a swimming gait to a crawling gait, characterized by a decreasing undulatory frequency (Fig. 7C) and an increasing curvature amplitude (Fig. 7F). We asked whether our model is consistent with this load-dependent gait adaptation.

We incorporated the effect of external viscosity into our model through the bending relaxation time constant τ_u (see *SI*). By varying viscosity η in the model, we generated corresponding oscillations and found that they are in quantitative agreement with previous results for frequency and amplitude dependence on viscosity of the external medium (Fig. 7 C,D).

The model generates a proprioceptive feedback variable in the form $P = K + b\dot{K}$ (Fig. 4A), and that the active muscle moment in our model undergoes a change of sign upon the proprioceptive feedback reaches either of two thresholds, P_{th} and $-P_{th}$. Given these, one would expect that, as the viscosity increases, a swimming worm will perform a slower undulation due to the external viscosity. That is, the term $b\dot{K}$ becomes

smaller. To compensate for this effect, the worm will undulate with a larger curvature amplitude such that the proprioceptive feedback would reach the fixed threshold for a switch in the muscle moment.

Next, we asked how the PRC depends on external viscosity. Model simulations with three different viscosities produced PRCs with similar sawtooth shape but with sharp transitions delayed in phase as the external viscosity increases (Fig. 7F). We also measured PRCs from optogenetic inhibition experiments in solutions of three different viscosities (Fig. 7G). Comparing the relative locations of the transitions in PRCs between the model and the data, our prediction also quantitatively agrees with the experimental results.

These results further support the model's description of how undulatory dynamics are modulated by the external environment.

Analysis of Alternative Models Supports a Relaxation Oscillation Mechanism

Although our computational model agrees well with our experimental results, we asked whether other models could also explain our findings. We examined three alternative models based on well-known mathematical descriptions of oscillators (van der Pol, Rayleigh, and Stuart-Landau oscillators) and compared them with our original threshold-switch model and with our experimental data (see *SI* and Figs. S7 and S8).

We found that of these models, our threshold-switch model produced the best overall agreement with experiments. We also found that two important experimental findings, the nonsinusoidal free-moving dynamics and the sawtooth-shaped PRCs can be achieved in our original model, the van der Pol and Rayleigh oscillators, which are all relaxation oscillators, but not in the Stuart-Landau oscillator, which is not a relaxation oscillator. These results support the notion that a relaxation oscillation mechanism underlies *C. elegans* motor rhythm generation.

Discussion

In this study, we used a combination of experimental and modeling approaches to probe the mechanisms underlying the *C. elegans* motor rhythm generation. In our model the mechanism for generating rhythmic patterns can be generally characterized by a 'relaxation oscillation' process which contains two alternating sub-processes on different time scales: a long relaxation process during which the motor system varies toward an intended state due to its biomechanics under a constant active muscle moment, alternating between a rapid period during which the active muscle moment switches to an opposite state due to a proprioceptive thresholding mechanism.

The term 'relaxation oscillation', as first employed by van der Pol, describes a general form of self-sustained oscillatory systems with intrinsic periodic relaxation/decay features (60). The Fitzhugh-Nagumo model (61, 62), a prototypical model of excitable neural systems, was originally derived by modifying the van der Pol relaxation oscillator equations. These and similar relaxation oscillators have been characterized in various dynamical systems in biology and neuroscience (54). For example, the dynamics exhibited from the action potentials of barnacle muscles in their oscillatory modes were found to yield 'push-pull' relaxation oscillation characteristics (63). The beating human heart was found to behave as a relaxation oscillator (64). Several studies of walking behavior in stick insects (65–68) proposed that the control system for rhythmic step movements constitutes a relaxation oscillator in which the transitions between leg movements is determined by proprioceptive thresholds.

Key properties shared by these relaxation oscillators are that their oscillations greatly differ from sinusoidal oscillations and that they all consist of a certain feedback loop with a 'discharging property': containing a switch component, that repetitively charges an integrating component until it reaches a threshold, then discharges it again (69). Many relaxation oscillators, including the van der Pol and Rayleigh models, exhibit sawtooth-shaped phase response curves (63; also see Figs. S7 and S8). As shown in our experimental and model results, all the above properties have been revealed in the dynamics of *C. elegans* locomotive behavior, consistent with the idea that the worm's rhythmic locomotion also results from a type of relaxation oscillator.

In our computational model, a proprioceptive component sensing the organism's changes in posture is required to generate adaptive locomotory rhythms. What elements in the motor system could be providing this

feedback? Previous studies have suggested that head and body motor neurons, including the SMDD head motor neurons and the B-type motor neurons, have proprioceptive capabilities (11, 39) and may also be involved in locomotory rhythm generation (37, 38, 40, 70). This possibility is consistent with earlier hypothesis that the long undifferentiated processes of these cholinergic neurons may function as proprioceptive sensors (24). In particular, recent findings (39) have revealed that SMDD neurons directly sense head muscle stretch and regulate muscle contractions during oscillatory head bending movements.

In our model, the proprioceptive feedback variable depends on both the curvature and the rate of change of curvature. Many mechanoreceptors are sensitive primarily to time derivatives of mechanical strain rather than strain itself; for example, the *C. elegans* touch receptor cells exhibit such a dependence (71, 72). The ability of mechanosensors to sense the rate of change in *C. elegans* curvature has been proposed in an earlier study (73) in which it was hypothesized that the B-type motor neurons might function as a proprioceptive component in this manner.

Further identification of the neuronal substrates for proprioceptive feedback may be possible through physiological studies of neuron and muscle activity using calcium or voltage indicators. Studies of the effect of targeted lesions and genetic mutations on the phase response curves will also help elucidate roles of specific neuromuscular components within locomotor rhythm generation.

In summary, our work describes the dynamics of the *C. elegans* locomotor system as a relaxation oscillation mechanism. Our model of rhythm generation mechanism followed from a quantitative characterization of free behavior and response to external disturbance, information closely linked to the structure of the animal's motor system (57, 74–76). Our findings represent an important step toward an integrative understanding of how neural and muscle activity, sensory feedback control, and biomechanical constraints generate locomotion.

Materials and Methods

Worm Strains and Cultivation. *C. elegans* were cultivated on NGM plates with *Escherichia coli* strain OP50 at 20°C using standard methods (77). Strains used and the procedure for optogenetic experiments are described in *SI.* Preparation of OP50 and OP50-ATR plates were as previously described (38). All experiments were performed with young adult (< 1 day) hermaphrodites which were synchronized by hypochlorite bleaching.

Locomotion and phase response analyses. To perform quantitative recordings of worm behavior we used a custom-built optogenetic targeting system as previously described (38, 53). Analysis of images for worm's body posture was performed using custom MATLAB (MathWorks) software. The anterior curvature is defined as the average of the curvature over body coordinate 0.1-0.3; this range avoided high frequency movements of the anterior tip of the animal. Descriptions of the apparatus and image analyses are available in *SI*.

For phase response experiments, *NpHR*-expressing worms were illuminated using a brief laser pulse (532 nm wavelength, 0.1 s duration, irradiance 16 mW/mm^2) in the head region (0-0.25 body coordinate). A total of 10 trials with 6 s interval between successive pulses were performed for each animal. Trials in which the worms did not maintain forward locomotion were censored. To generate the phase response curve (PRC), we calculated the phase of inhibition of each trial and the resulting phase shift. Further statistical manipulations were performed to obtain the averaged representations of the PRC. Details for these calculations are given in *SI*.

Computational Modeling. Our primary model is based on a novel neural control mechanism incorporated with a previously described biomechanical framework (47, 50, 51). A proprioceptive signal is defined by a linear combination of bending curvature and rate of change of curvature. When the signal reaches a threshold, a switching command is initiated to reverse the direction of muscle moment. The worm's curvature relaxes toward the opposite direction, and the process repeats, creating a dorsoventral oscillation. Detailed descriptions of implementation and fitting procedure of this model and alternative models are available in *SI*.

Acknowledgments

We thank Mei Zhen and Quan Wen for providing strains. Some strains were provided by the CGC, funded by NIH Office of Research Infrastructure Programs (P40 OD010440). H.J., A.D.F, and C.F.-Y. were supported by the National Institutes of Health (1R01NS084835). S.T. was supported by an Abraham Noordergraaf Research Fellowship and a Littlejohn Fellowship. We thank Gal Haspel, Michael Carchidi, and Patrick McClanahan for helpful discussions.

References

1. O. Kiehn, *Neuronal mechanisms for generating locomotor activity* (New York Academy of Sciences, 1998) (June 2, 2020).

2. S. Grillner, P. Wallen, Cellular bases of a vertebrate locomotor system–steering, intersegmental and segmental co-ordination and sensory control. *Brain research reviews* **40**, 92–106 (2002).

3. A. Borgmann, S. L. Hooper, A. Büschges, Sensory feedback induced by front-leg stepping entrains the activity of central pattern generators in caudal segments of the stick insect walking system. *Journal of Neuroscience* **29**, 2972–2983 (2009).

4. S. Grillner, The motor infrastructure: from ion channels to neuronal networks. *Nature Reviews Neuroscience* **4**, 573–586 (2003).

5. O. Kiehn, Development and functional organization of spinal locomotor circuits. *Current opinion in neurobiology* **21**, 100–109 (2011).

6. E. Marder, R. L. Calabrese, Principles of rhythmic motor pattern generation. *Physiological reviews* **76**, 687–717 (1996).

7. A. H. Cohen, P. Wallén, The neuronal correlate of locomotion in fish. *Experimental brain research* **41**, 11–18 (1980).

8. R. A. Pearce, W. O. Friesen, Intersegmental coordination of leech swimming: comparison of in situ and isolated nerve cord activity with body wall movement. *Brain research* **299**, 363–366 (1984).

9. W. B. Kristan, R. L. Calabrese, Rhythmic swimming activity in neurones of the isolated nerve cord of the leech. *Journal of Experimental Biology* **65**, 643–668 (1976).

10. X. Yu, B. Nguyen, W. O. Friesen, Sensory feedback can coordinate the swimming activity of the leech. *Journal of Neuroscience* **19**, 4634–4643 (1999).

11. Q. Wen, *et al.*, Proprioceptive coupling within motor neurons drives C. elegans forward locomotion. *Neuron* **76**, 750–761 (2012).

12. W. O. Friesen, Central Pattern Generators: Sensory Feedback. Encyclopedia of Neuroscience (2009).

13. K. G. Pearson, “Generating the walking gait: role of sensory feedback” in *Progress in Brain Research*, (Elsevier, 2004), pp. 123–129.

14. O. J. Mullins, J. T. Hackett, J. T. Buchanan, W. O. Friesen, Neuronal control of swimming behavior: comparison of vertebrate and invertebrate model systems. *Progress in neurobiology* **93**, 244–269 (2011).

15. P. D. Brodfuehrer, W. O. Friesen, From stimulation to undulation: a neuronal pathway for the control of swimming in the leech. *Science* **234**, 1002–1004 (1986).

16. O. Andersson, H. Forssberg, S. Grillner, P. Wallen, Peripheral feedback mechanisms acting on the central pattern generators for locomotion in fish and cat. *Canadian journal of physiology and pharmacology* **59**, 713–726 (1981).

17. Ö. Ekeberg, S. Grillner, Simulations of neuromuscular control in lamprey swimming. *Philosophical Transactions of the Royal Society of London. Series B: Biological Sciences* **354**, 895–902 (1999).

18. J. Cang, W. O. Friesen, Sensory modification of leech swimming: rhythmic activity of ventral stretch receptors can change intersegmental phase relationships. *Journal of Neuroscience* **20**, 7822–7829 (2000).

19. J. Cang, X. Yu, O. W. Friesen, Sensory modification of leech swimming: interactions between ventral stretch receptors and swim-related neurons. *Journal of Comparative Physiology A* **187**, 569–579 (2001).

20. C. S. Mendes, I. Bartos, T. Akay, S. Márka, R. S. Mann, Quantification of gait parameters in freely walking wild type and sensory deprived Drosophila melanogaster. *elife* **2**, e00231 (2013).

21. B. Akitake, *et al.*, Coordination and fine motor control depend on Drosophila TRPγ. *Nature communications* **6**, 1–13 (2015).

22. X. Yu, W. O. Friesen, Entrainment of leech swimming activity by the ventral stretch receptor. *Journal of Comparative Physiology A* **190**, 939–949 (2004).

23. S. Grillner, A. McClellan, C. Perret, Entrainment of the spinal pattern generators for swimming by mechano-sensitive elements in the lamprey spinal cord in vitro. *Brain research* **217**, 380–386 (1981).

24. J. G. White, E. Southgate, J. N. Thomson, S. Brenner, The structure of the nervous system of the nematode Caenorhabditis elegans. *Philos Trans R Soc Lond B Biol Sci* **314**, 1–340 (1986).

25. S. J. Cook, *et al.*, Whole-animal connectomes of both Caenorhabditis elegans sexes. *Nature* **571**, 63–71 (2019).

26. S. Brenner, The genetics of Caenorhabditis elegans. *Genetics* **77**, 71–94 (1974).

27. C. I. Bargmann, Neurobiology of the Caenorhabditis elegans genome. *Science* **282**, 2028–2033 (1998).

28. O. Hobert, Behavioral plasticity in C. elegans: paradigms, circuits, genes. *Journal of neurobiology* **54**, 203–223 (2003).

29. N. A. Croll, The behaviour of nematodes: their activity, senses and responses. *The behaviour of nematodes: their activity, senses and responses.* (1970).

30. M. Chalfie, *et al.*, The neural circuit for touch sensitivity in Caenorhabditis elegans. *Journal of Neuroscience* **5**, 956–964 (1985).

31. S. L. McIntire, E. Jorgensen, J. Kaplan, H. R. Horvitz, The GABAergic nervous system of Caenorhabditis elegans. *Nature* **364**, 337–341 (1993).

32. L. Deng, *et al.*, Inhibition underlies fast undulatory locomotion in C. elegans. *bioRxiv* (2020).

33. M. Chalfie, J. White, W. B. Wood, *The nematode Caenorhabditis elegans* (New York: Cold Spring Harbor Laboratory Press, 1988).

34. M. Driscoll, J. Kaplan, Mechanotransduction (1997).

35. S. E. Von Stetina, M. Treinin, D. M. Miller, The motor circuit. *Int. Rev. Neurobiol* **69**, 125–167 (2006).

36. T. Kawano, *et al.*, An imbalancing act: gap junctions reduce the backward motor circuit activity to bias C. elegans for forward locomotion. *Neuron* **72**, 572–586 (2011).

37. S. Gao, *et al.*, Excitatory motor neurons are local oscillators for backward locomotion. *Elife* **7**, e29915 (2018).

38. A. D. Fouad, *et al.*, Distributed rhythm generators underlie Caenorhabditis elegans forward locomotion. *Elife* **7**, e29913 (2018).

39. J. Yeon, *et al.*, A sensory-motor neuron type mediates proprioceptive coordination of steering in C. elegans via two TRPC channels. *PLoS biology* **16**, e2004929 (2018).

40. H. S. Kaplan, O. S. Thula, N. Khoss, M. Zimmer, Nested neuronal dynamics orchestrate a behavioral hierarchy across timescales. *Neuron* **105**, 562–576 (2020).

41. W. Li, Z. Feng, P. W. Sternberg, X. S. Xu, A C. elegans stretch receptor neuron revealed by a mechanosensitive TRP channel homologue. *Nature* **440**, 684–687 (2006).

42. L. Tao, *et al.*, Parallel Processing of Two Mechanosensory Modalities by a Single Neuron in C. elegans. *Developmental cell* **51**, 617–631 (2019).

43. E. Niebur, P. Erdös, Theory of the locomotion of nematodes: dynamics of undulatory progression on a surface. *Biophysical journal* **60**, 1132–1146 (1991).

44. J. Karbowski, G. Schindelman, C. J. Cronin, A. Seah, P. W. Sternberg, Systems level circuit model of C. elegans undulatory locomotion: mathematical modeling and molecular genetics. *Journal of computational neuroscience* **24**, 253–276 (2008).

45. J. Bryden, N. Cohen, Neural control of Caenorhabditis elegans forward locomotion: the role of sensory feedback. *Biological cybernetics* **98**, 339–351 (2008).

46. S. Berri, J. H. Boyle, M. Tassieri, I. A. Hope, N. Cohen, Forward locomotion of the nematode C. elegans is achieved through modulation of a single gait. *HFSP journal* **3**, 186–193 (2009).

47. C. Fang-Yen, *et al.*, Biomechanical analysis of gait adaptation in the nematode Caenorhabditis elegans. *Proceedings of the National Academy of Sciences* **107**, 20323–20328 (2010).

48. J. H. Boyle, S. Berri, N. Cohen, Gait modulation in C. elegans: an integrated neuromechanical model. *Frontiers in computational neuroscience* **6**, 10 (2012).

49. L. B. Sheiner, S. L. Beal, Some suggestions for measuring predictive performance. *Journal of pharmacokinetics and biopharmaceutics* **9**, 503–512 (1981).

50. H. R. Wallace, The dynamics of nematode movement. *Annual Review of Phytopathology* **6**, 91–114 (1968).

51. J. Gray, H. W. Lissmann, The locomotion of nematodes. *Journal of Experimental Biology* **41**, 135–154 (1964).

52. J. T. Pierce-Shimomura, *et al.*, Genetic analysis of crawling and swimming locomotory patterns in C. elegans. *Proceedings of the National Academy of Sciences* **105**, 20982–20987 (2008).

53. A. M. Leifer, C. Fang-Yen, M. Gershow, M. J. Alkema, A. D. Samuel, Optogenetic manipulation of neural activity in freely moving Caenorhabditis elegans. *Nature methods* **8**, 147–152 (2011).

54. E. M. Izhikevich, *Dynamical systems in neuroscience* (MIT press, 2007).

55. Z. V. Guo, L. Mahadevan, Limbless undulatory propulsion on land. *Proceedings of the National Academy of Sciences* **105**, 3179–3184 (2008).

56. J. Gray, Studies in animal locomotion: I. The movement of fish with special reference to the eel. *Journal of experimental biology* **10**, 88–104 (1933).

57. N. W. Schultheiss, A. A. Prinz, R. J. Butera, *Phase response curves in neuroscience: theory, experiment, and analysis* (Springer Science & Business Media, 2011).

58. B. Pietras, A. Daffertshofer, Network dynamics of coupled oscillators and phase reduction techniques. *Physics Reports* (2019).

59. M. Rosenblum, Inferring the phase response curve from observation of a continuously perturbed oscillator. *Scientific reports* **8**, 1–10 (2018).

60. B. Van der Pol, LXXXVIII. On “relaxation-oscillations.” *The London, Edinburgh, and Dublin Philosophical Magazine and Journal of Science* **2**, 978–992 (1926).

61. R. FitzHugh, Impulses and physiological states in theoretical models of nerve membrane. *Biophysical journal* **1**, 445 (1961).

62. J. Nagumo, S. Arimoto, S. Yoshizawa, An active pulse transmission line simulating nerve axon. *Proceedings of the IRE* **50**, 2061–2070 (1962).

63. C. Morris, H. Lecar, Voltage oscillations in the barnacle giant muscle fiber. *Biophysical journal* **35**, 193–213 (1981).

64. B. VAN DER POL, Biological rhythms considered as relaxation oscillations. *Acta Medica Scandinavica* **103**, 76–88 (1940).

65. G. Wendler, Ein Analogmodell der Beinbewegungen eines laufenden Insekts. *Kybernetik* **18**, 68–74 (1968).

66. U. Bässler, Sensory control of leg movement in the stick insect Carausius morosus. *Biological cybernetics* **25**, 61–72 (1977).

67. D. Graham, “Pattern and control of walking in insects” in *Advances in Insect Physiology*, (Elsevier, 1985), pp. 31–140.

68. H. Cruse, The control of body position in the stick insect (Carausius morosus), when walking over uneven surfaces. *Biological Cybernetics* **24**, 25–33 (1976).

69. C. R. Nave, *Relaxation oscillator concept* (1995).

70. T. Xu, *et al.*, Descending pathway facilitates undulatory wave propagation in Caenorhabditis elegans through gap junctions. *Proceedings of the National Academy of Sciences* **115**, E4493–E4502 (2018).

71. R. O’Hagan, M. Chalfie, M. B. Goodman, The MEC-4 DEG/ENaC channel of Caenorhabditis elegans touch receptor neurons transduces mechanical signals. *Nature neuroscience* **8**, 43–50 (2005).

72. A. L. Eastwood, *et al.*, Tissue mechanics govern the rapidly adapting and symmetrical response to touch. *Proceedings of the National Academy of Sciences* **112**, E6955–E6963 (2015).

73. V. J. Butler, *et al.*, A consistent muscle activation strategy underlies crawling and swimming in Caenorhabditis elegans. *Journal of the Royal Society Interface* **12**, 20140963 (2015).

74. B. S. Gutkin, G. B. Ermentrout, A. D. Reyes, Phase-response curves give the responses of neurons to transient inputs. *Journal of neurophysiology* **94**, 1623–1635 (2005).

75. R. M. Smeal, G. B. Ermentrout, J. A. White, Phase-response curves and synchronized neural networks. *Philosophical Transactions of the Royal Society B: Biological Sciences* **365**, 2407–2422 (2010).

76. F. Nadim, S. Zhao, A. Bose, “A PRC description of how inhibitory feedback promotes oscillation stability” in *Phase Response Curves in Neuroscience*, (Springer, 2012), pp. 399–417.

77. J. Sulston, J. Hodgkin, The nematode Caenorhabditis elegans (1988).

Figures

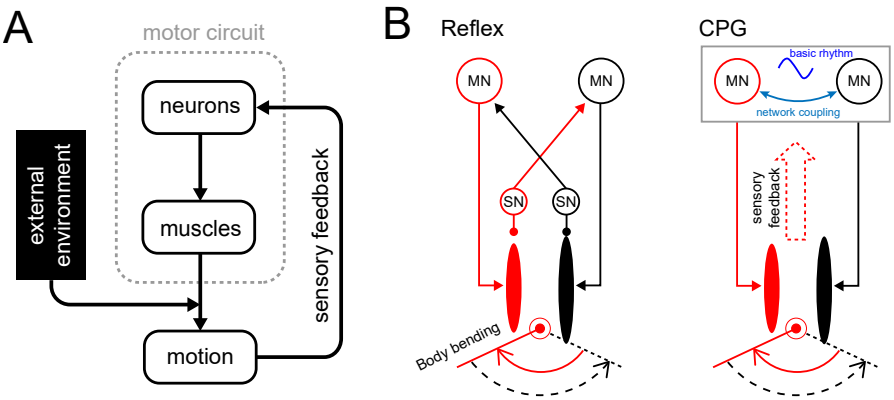

Figure 1. Rhythm generation in *C. elegans*. (A) Motor neurons generate patterned neuronal signals to control the activation of muscles, which generates movement subject to the constraints of the external environment and internal biomechanics. Sensory feedback stabilizes and modulates the rhythms. (B) Two possible models for locomotory rhythm generation in *C. elegans*. In a reflex loop model (*left*) sensory neurons (SN) detect body postures and excite motor neurons (MN) to activate the antagonist body wall muscles. In a central pattern generator (CPG) model (*right*) network of motor neurons generates basic rhythmic activities that are transmitted to antagonist body wall muscles and the sensory feedback modulates the CPG rhythm. The diagrams are adapted from Marder and Bucher, 2001.

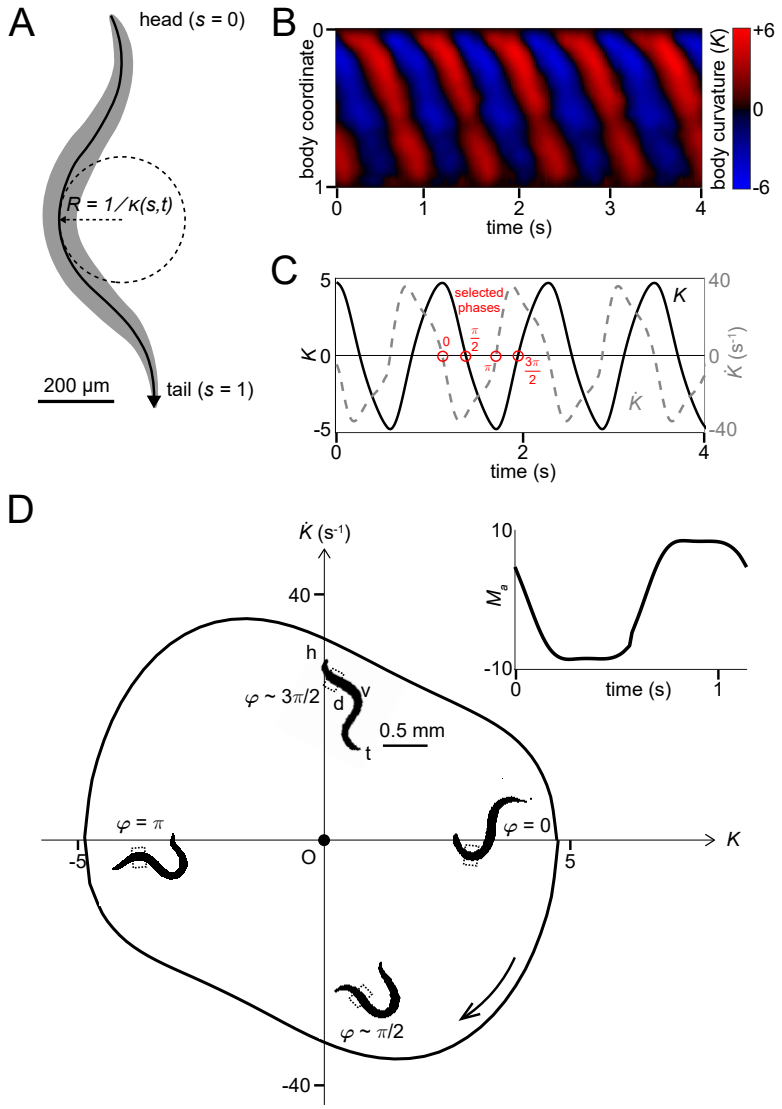

Figure 2. Undulatory dynamics of freely moving worms. (A) Worm undulatory dynamics are quantified by the time-varying curvature along the body. The normalized body coordinate is defined by the fractional distance from the head (head = 0; tail = 1) along a centerline. The curvature κ is the reciprocal of the local radius of curvature. (B) Curvature as a function of time and body coordinate during forward movement in a viscous liquid. Body bending K is represented using the nondimensional product of κ and body length L. (C) Curvature (black) in the anterior region (0.1-0.3 body coordinate) and the time derivative (dashed grey) of this curvature. Red circles mark four representative phases (0, $\pi/2$, π, and $3\pi/2$). The curve is an average of 5041 locomotion cycles from 116 worms. (D) Phase portrait representation of the oscillatory dynamics, showing the curvature and the time derivative of the curvature parameterized by time. Images of worm correspond to the phases marked in C. Arrow indicates clockwise movement. (*Inset*) waveform of the scaled active muscle moment, estimated by equation $M_a = K + \tau_u \dot{K}$. Both curves were computed from the data used in C.

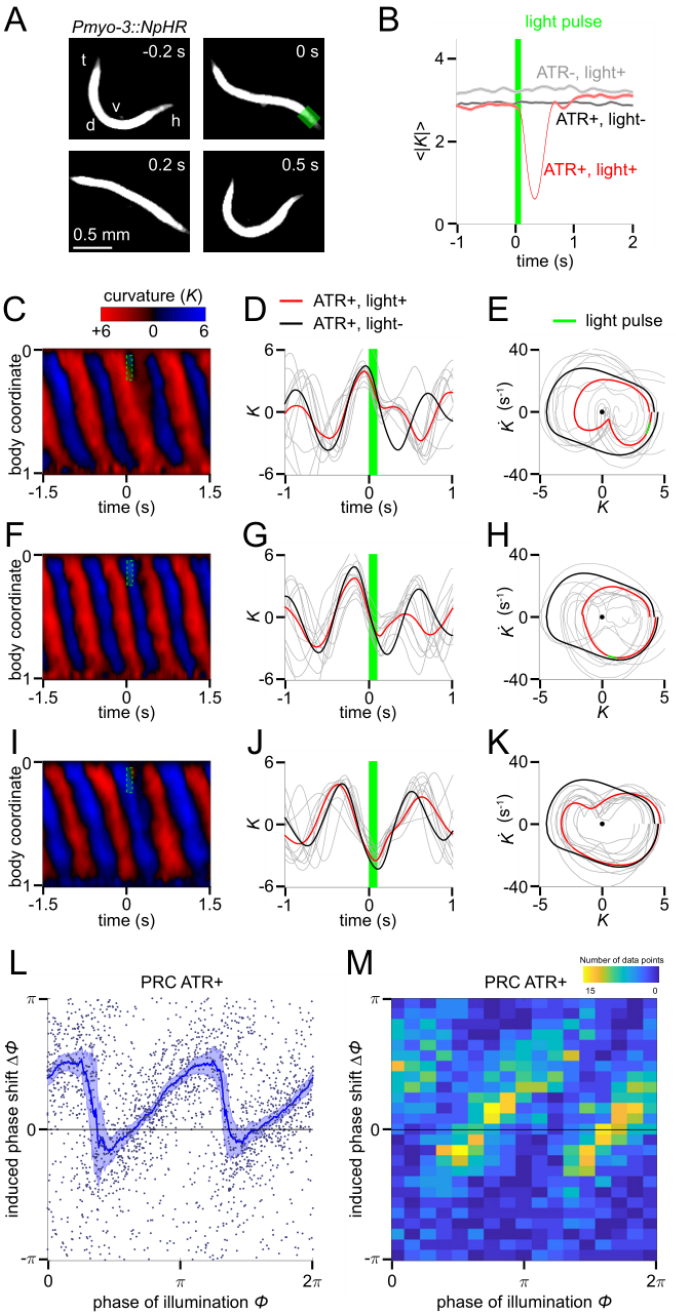

Figure 3. Analysis of phase-dependent inhibitions of oscillations using transient optogenetic muscle inhibition. (A) Images of a transgenic worm (*Pmyo-3::NpHR*) perturbed by a transient optogenetic muscle inhibition during its normal locomotion. The green bar indicates a 0.1-sec interval during which the head was illuminated by a laser (532 nm wavelength). (B) Effect of muscle inhibitions on mean absolute curvatures $|K|$ of the head region. Black curve represents control ATR+ (no light) group (3523 measurements using 337 worms), and grey curve represents control ATR- group which was not affected by green light (2072 measurements using 116 worms), whereas red curve represents ATR+ group (1910 measurements using 337 worms). Green bar indicates 0.1-sec light illumination starting at $t = 0$. (C-E) Perturbed dynamics around light pulses occurring in the phase range $[0, \pi/6]$. (C) Kymogram of time-varying curvature K around a short inhibition (green dashed-outlined box). (D) Mean curvature dynamics around the inhibitions (green bar, aligned at $t = 0$) from ATR+ group (red curve, 11 trials using 4 worms) and control ATR+ (no light) group (black curve, 8 trials using 3 worms). Grey curves are individual trials from ATR+ group (10 randomly selected trials are shown). (E) Mean

phase portrait graphs around the inhibitions (green line) from ATR+ group (same trials as in D) and control group (ATR+, no light, 3998 trials using 337 worms). Grey curves are individual trials from ATR+ group. (F-H) Similar to C-E, for phase range $[\pi/3, \pi/2]$. (I-K) Similar to C-E, for phase range $[2\pi/3, 5\pi/6]$. (L) A curve representation of the PRC from optogenetic inhibition experiments (ATR+ group, 991 trials using 337 worms, each point indicating a single illumination of one worm). The curve was obtained via a moving average along the *x*-axis with 0.16π in bin width and the filled area represents 95% confidence interval within the bin. (M) A histogram representation of the PRC using the same data. The histogram uses 25 bins for both dimensions, and the color indicates the number of data points within each rectangular bin.

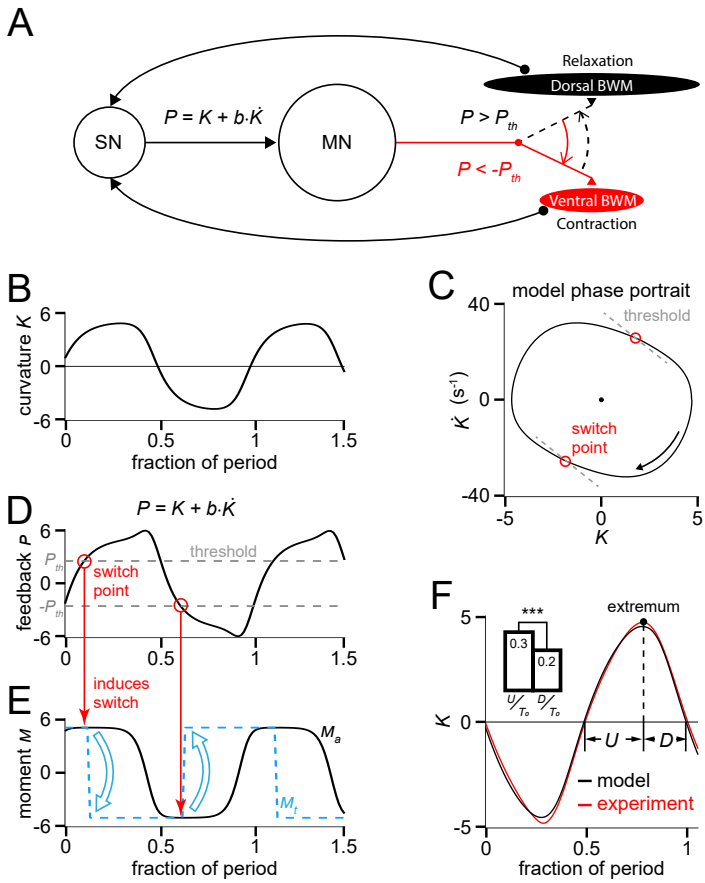

Figure 4. Free-running dynamics of a bidirectional relaxation oscillator model. (A) Schematic diagram of the relaxation oscillator model. In this model, sensory neurons (SN) detect the total curvature of the body segment as well as the time derivative of the curvature. The linear combination of the two values, $P = K + b\dot{K}$, is modeled as the proprioceptive signal which is transmitted to motor neurons (MN). The motor neurons alternatingly activate dorsal or ventral body wall muscles based on a thresholding rule: (1) if $P < -P_{th}$, the ventral body wall muscles get activated and contract while the dorsal side of muscles relax; (2) if $P > P_{th}$, vice versa. Hence, locomotion rhythms are generated from this threshold-switch process. (B) Time-varying curvature K of the model oscillator. The time axis is normalized with respect to oscillatory period (same for D, E, and F). (C) Phase portrait graph of the model oscillator. Proprioceptive threshold lines (grey dashed lines) intersect with the phase portrait graph at two switch points (red circles) at which the active moment of body wall muscles is switched. (D) Time-varying proprioceptive feedback P received by the motor neurons. Horizontal lines denote the proprioceptive thresholds (grey dashed lines) that switch the active moment of body wall muscles at switch points (red circles, intersections between the proprioceptive feedback curve and the threshold lines). (E) Time-varying active moment of body wall muscles. Blue-dashed square wave denotes target moment (M_t) that instantly switches directions at switch points. Black curve denotes the active moment of body wall muscles (M_a) which follows the target moment in a delayed manner. (F) Time varying curvature in worm's head region from experiments (red, 5047 cycles using 116 worms) and model (black). Model curvature matches experimental curvature with an MSE ≈ 0.18. (*Inset*) Bar graph of U (time period of bending toward the ventral or dorsal directions) and D (time period of straightening toward a straight posture). Vertical bars are averages of fractions with respect to T_0 (undulatory period) of U and T (*** indicates p<0.0005 using Student's *t* test).

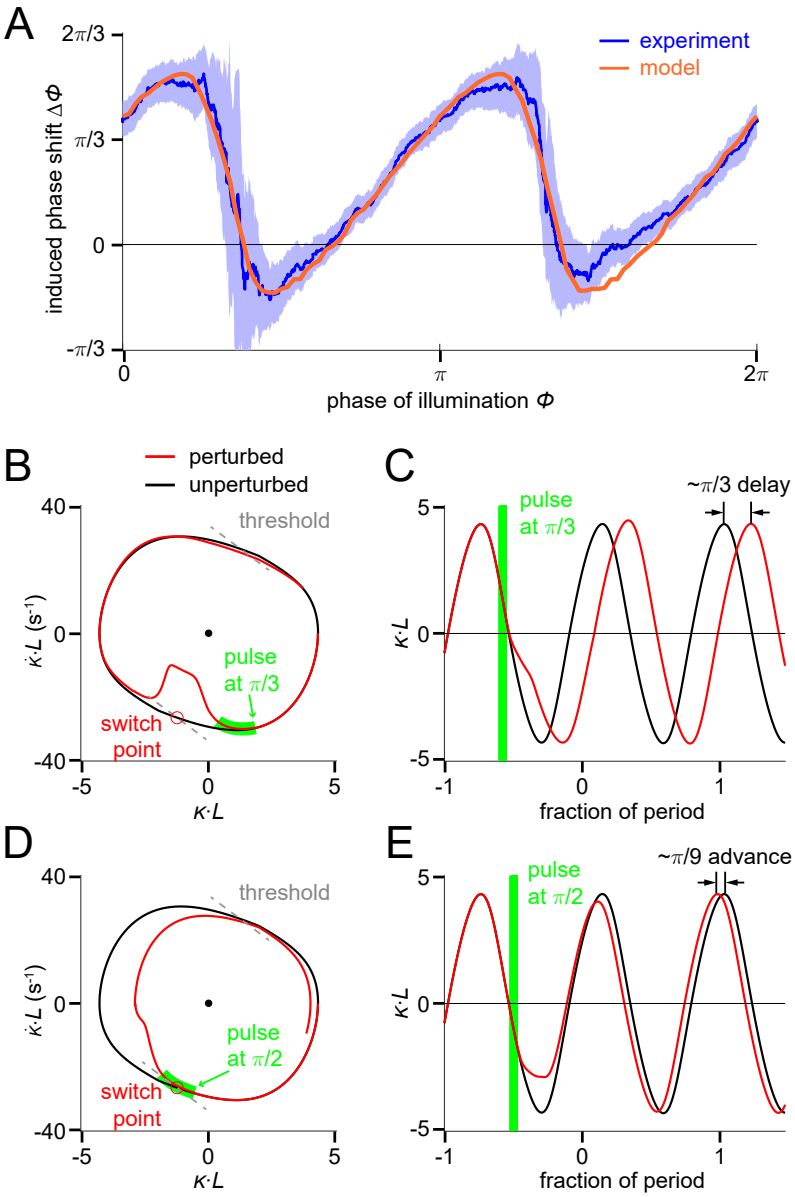

Figure 5. Simulations of optogenetic inhibitions in the relaxation oscillator model. (A) Phase response curves measured from experiments (blue, same as in Fig. 3L) and model (orange). Model PRC matches experimental PRC with an MSE ≈ 0.12. (B,C) Simulated dynamics of locomotion showing inhibition-induced phase delays in the model oscillator. (B) Simulated phase portrait graphs around inhibition occurring at $\pi/6$ phase of cycle for perturbed (red) and unperturbed (black) dynamics. Green bar indicates the phase during which the inhibition occurs. (C) Same dynamics as in B, represented by time-varying curvatures. (D,E) Simulated dynamics of locomotion showing inhibition-induced phase advances in the model oscillator. (D) Simulated phase portrait graphs around inhibition occurring at $\pi/2$ phase of cycle for perturbed (red) and unperturbed (black) dynamics. (E) Same dynamics as in D, represented by time-varying curvatures.

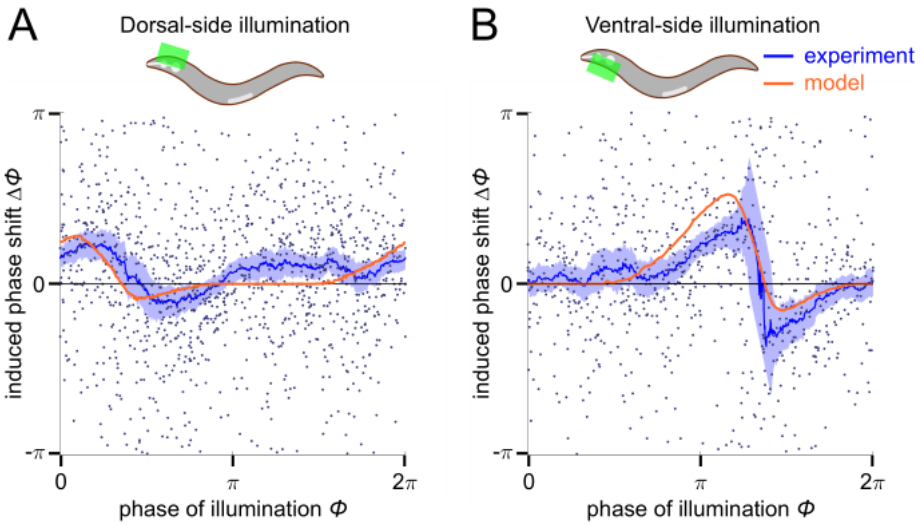

Figure 6. The model predicts phase response curves with respect to single-side muscle inhibitions. (A) (*Upper*) a cartoon indicating a transient inhibition of body wall muscles of the head on the dorsal side. (*Lower*) the corresponding PRC measured from experiments (blue, 576 trials using 242 worms) and model (orange). (B) (*Upper*) a cartoon indicating a transient inhibition of body wall muscles of the head on the ventral side. (*Lower*) the corresponding PRC measured from experiments (blue, 373 trials using 176 worms) and model (orange). For the two experiments, each point indicates a single illumination (0.1 s duration, 532 nm wavelength) of one worm. Experimental curves were obtained using a moving average along the *x*-axis with 0.16π in bin width. Filled area of each experimental curve represents 95% confidence interval with respect to each bin of data points.

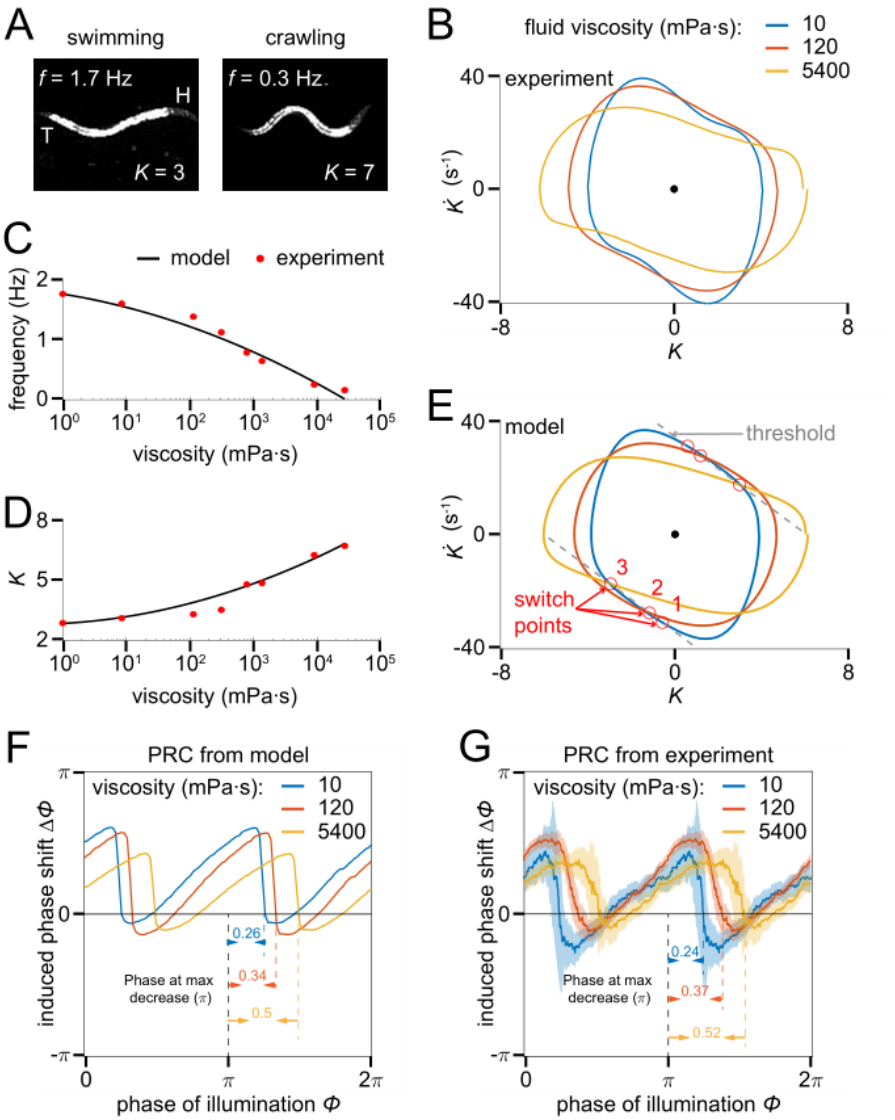

Figure 7. Model reproduces *C. elegans* gait adaptation to external viscosity. (A) Dark field images and the corresponding undulatory frequencies and amplitudes of adult worms (*left*) swimming in NGM buffer of viscosity 1 mPa·s, (*right*) crawling on agar gel surface. The worm head is to the right in both images. (B) Phase portrait graphs measured from worm normal movements in fluids of viscosity 10 mPa·s (blue, 3528 cycles using 50 worms), 120 mPa·s (red, 5050 cycles using 116 worms), and 5400 mPa·s (yellow, 1364 cycles using 70 worms). (C,D) The model predicts the dependence of undulatory frequency (C) and curvature amplitude (D) on external viscosity (black) that closely fit the corresponding experimental observations (red). (E) Phase portrait graphs predicted from the model in three different viscosities (same values as in B). Grey dashed lines indicate threshold lines for dorsal-ventral bending. The intersections (red circles 1, 2, 3) between the threshold line and phase portrait graphs are switch points for undulations in low, medium, high viscosity, respectively. (F) Theoretically predicted PRCs in fluids of the three different viscosities show that PRC will be shifted to the right as the viscosity of environment increases. (G) PRCs measured from optogenetic inhibition experiments in the three viscosities. Experimental PRC curves were obtained using a moving average along the *x*-axis with 0.16π in bin width and filled areas are 95% confidence interval. The tendency of shift observed in experimental PRCs verified the model prediction.

Supporting Information for
Phase response analyses support a relaxation oscillator model of locomotor rhythm generation in Caenorhabditis elegans

Supplemental Results

Phase Response Curves for Optogenetic Inhibition of Cholinergic and GABAergic Neurons

The GABAergic D-type motor neurons provide a dorsoventral cross-inhibition pattern to avoid simultaneous contraction of both sides of muscles during normal locomotion. We therefore asked whether the D-type motor neurons are critical for the sawtooth feature of the PRC. We examined transgenic worms that express *NpHR* in the body wall muscles but lack the GABA receptor required by the D-type motor neurons (1). After performing the optogenetic inhibition experiments, we found that the PRC of this strain also displays a sawtooth feature (Fig. S2). This result shows that D-type motor neurons are not necessary for motor rhythm generator to show the particular PRC.

Besides examining PRCs induced by muscle inhibition, we also tested animal's PRCs with respect to specific inhibitions of cholinergic neurons. To do this, we examined transgenic worms in which either all cholinergic neurons or B-type motor neurons are expressing the inhibitory opsin (*Punc-17::NpHR::ECFP* and *Pacr-5 Arch-mCherry*, respectively). From the optogenetic inhibition experiments of the two transgenic strains, we again observed sawtooth-shaped PRCs (Figs. S2 and S3, respectively), with variations only in the values of phase shifts.

Analysis of Alternative Models

We examined three alternative models based on well-known mathematical descriptions of oscillators (van der Pol, Rayleigh, and Stuart-Landau oscillators) and compared them with our original threshold-switch model and with our experimental data (Figs. S7 and S8).

In order to explicitly compare these alternative models with our original model and experimental data, we tested in detail the waveforms and phase plots of their limit cycles where systems are stable and unperturbed, and examined their PRCs with respect to transient muscle inhibition via computational simulations (see *Supplemental Materials and Methods*).

First, we tested the van der Pol oscillator, the first relaxation oscillator model (2) which has long been applied in modeling neuronal dynamics (3, 4). It is based on a second-order differential equation for a harmonic oscillator with a nonlinear, displacement-dependent damping term (*Supplemental Materials and Methods*). By choosing a set of appropriate parameters (*Supplemental Materials and Methods*), we found that the free-running waveform and phase plot of the van der Pol oscillator are highly asymmetric, but in an inverted manner (Fig. S7 A,D), compared with the experimental observations (Fig. 4 C,F). Transiently perturbing the system with the bell-shaped modulatory function over the phase of a cycle produced a similar sawtooth-shaped PRC as that observed experimentally (Fig. S7J). However, the perturbed system was shown to recover toward its limit cycle with a much slower rate than that of the experiments (Fig. S7G). Simulations of single-side muscle inhibitions to the system produced single-sawtooth-shaped PRCs similar to those found experimentally (Fig. S8 A,D).

Next, we examined the Rayleigh oscillator, another relaxation oscillator model which was originally proposed to describe self-sustained acoustic vibrations such as vibrating clarinet reeds (5). It is based on a second-order differential equation with a nonlinear, velocity-dependent damping term and it can be obtained from the van der Pol oscillator via a variable differentiation and substitution (*Supplemental Materials and Methods*). From its free-running dynamics, we observed that the system exhibits a highly asymmetric waveform and phase plot that are similar to the experimental observations (Fig. S7 B,E). Additionally, the Rayleigh oscillator also produces similar sawtooth-shaped PRCs with respect to transient muscle inhibitions of both sides (Fig. S7K), dorsal side (Fig. S8B), and ventral side (Fig. S8E), respectively, and system's recovery rate after the perturbation was shown to be more similar to that of the experiments (Fig. S7H).

Finally, we considered the Stuart-Landau oscillator, a commonly used model for the analysis of neuronal synchrony (6). Its nonlinearity is based on a negative damping term which depends on the magnitude of the

state variable defined in a complex domain (*Supplemental Materials and Methods*). Due to its property, the negative damping of the system would constantly neutralize the positive damping on a limit cycle, making its free-running dynamics a harmonic oscillation which shows a sinusoidal waveform (Fig. S7 C,F). Moreover, the PRC with respect to transient muscle inhibitions is constant (Fig. S7L), contrary to the experiments.

These simulation results show that the nonsinusoidal free-running dynamics and the sawtooth-shaped PRCs observed from experiments can be achieved in our original model, the van der Pol and Rayleigh oscillators, which are all relaxation oscillators, but not in the Stuart-Landau oscillator, which is not a relaxation oscillator. These results support the notion that a relaxation-oscillation mechanism underlies C. elegans motor rhythm generation.

Supplemental Materials and Methods

Strains and Plates Preparations

Transgenic strains used in this study are listed as follows: YX148 *qhIs1[Pmyo-3::NpHR::eCFP; lin-15(+)];qhIs4[Pacr-2::wCherry],* YX119 *unc-49(e407);lin-15(n765ts);qhIs1[Pmyo-3::NpHR::eCFP;lin-15(+)],* YX205 *hpIs178[Punc-17::NpHR::eCFP;lin-15(+)],* WEN001 *wenIs001[Pacr-5::Arch::mCherry].*

For optogenetic experiments, worms were cultivated in darkness on plates with OP50 containing the cofactor all-*trans* retinal (ATR). For control experiments and free-moving experiments, worms were cultivated on regular OP50 NGM plates without ATR. To make OP50-ATR plates, we added 2 μL of a 100 mM solution of ATR in ethanol to an overnight culture of 250 μL OP50 in LB medium and used this mixture to seed 6 cm NGM plates.

Locomotion Analysis

To analyze worm locomotion in viscous fluids, we placed worms in dextran solutions in chambers formed by a glass slide and a coverslip separated by 125-μm-thick plastic shims. For viscosity-dependence experiments, we used 5%, 17%, and 35% (by mass) solutions of dextran (Sigma-Aldrich D5376, average molecular weight 1,500,000-2,800,000) in NGMB. These solutions were measured to have viscosities of 10, 120, and 5400 mPa·s (7), respectively. We used a 17% dextran solution for all other experiments. NGMB consists of the same components as NGM media (8), but without agar, peptone, or cholesterol.

We recorded image sequences using a custom-built optogenetic targeting system based on a Leica DMI4000B microscope under 10X magnification with dark field illumination provided by red LEDs. Worm images were recorded at 40 Hz with a sCMOS camera (Teledyne Photometrics optiMOS). We used custom-written C++ software (9) to perform real-time segmentation of the worm during image acquisition. The worm was identified in each image by its boundary and centerline calculated from a binary image. Anterior-posterior orientation was noted visually during the recording. Segmentation information, including coordinates of the worm boundary and centerline, was saved to disk along with the corresponding image sequences.

Post-acquisition image analysis was performed using MATLAB (Mathworks). The worm centerline of each image was smoothed using a cubic spline fit. We calculated curvature κ as the dot product between the unit normal vector to the centerline and derivative of the unit tangent vector to the centerline with respect to the body coordinate. Dimensionless curvature K was calculated as the product of κ and the worm body length L represented by length of the centerline. Since the segmentation was relatively noisy at the tips of the worm, we excluded curvature in the anterior and posterior 5% of the body length. The worm's direction of motion was identified by calculating the gradients in the curvature over time and body coordinate, and image sequences in which the worm performed consistent forward movement (lasting at least 4 s) were selected for analysis. The anterior curvature $K(t)$ was defined as the average of the dimensionless curvature over body coordinate 0.1-0.3; this range avoided high frequency movements of the anterior tip of the animal.

To quantify oscillatory dynamics during forward locomotion, we identified undulatory cycles from the time sequence of anterior curvature in each worm. Local extrema along each sequence were identified and portions between consecutive local maxima were defined as individual cycles. To minimize the effects of changes in the worm's frequency, we excluded cycles whose period deviated by more than 20% from the average period of all worms' undulations in each experimental session.

For the ease of computing average dynamics, we converted individual cycles from a time-dependent to a phase-dependent curvature by uniformly rescaling each cycle to a phase range of 2π. The averaged curvature within one cycle was then computed by averaging all individual cycles in the phase domain: $\langle K(\phi)\rangle = \sum_{i=1}^{N} K_i(\phi)\,/N$. Similarly, the averaged phase derivative of curvature within one cycle was calculated as $\langle dK/d\phi\rangle = \sum_{i=1}^{N}(dK_i/d\phi)\,/N$.

Phase Response Analysis

To generate phase response curves (PRCs) from optogenetic inhibition experiments, each trial's illumination phase ϕ, as well as the induced phase shift F, were calculated. To calculate the two variables, animal's phase of oscillation was estimated based on timings of local extrema identified from the time-varying curvature profiles via a peak finding method. Specifically, (i) the occurrence of illumination of the trial was set to $t = T_{illum}$; $t = 0$ was set at the beginning of each experiment. (ii) Around the illumination, timings of the two local maxima of curvature immediately before and after were identified as the two zero-phase points of the oscillation before and after the illumination, respectively. Here, the timings are denoted as TZ_{-2}, TZ_{-1}, TZ_{+1}, and TZ_{+2}, in the ascending order of time. (iii) Similarly, timings of the two local minima of curvature immediately before and after the illumination were identified as the two half-cycle-phase points before and after the illumination, respectively. Here, the timings are denoted as TH_{-2}, TH_{-1}, TH_{+1}, and TH_{+2}, in the ascending order of time. (iv) With these measurements, cycle period T_0 was computed as[1] $T_0 = (TZ_{+2} - TZ_{+1} + TZ_{-1} - TZ_{-2} + TH_{+2} - TH_{+1} + TH_{-1} - TH_{-2})/4$, so the angular frequency of undulation $\omega_0 = 2\pi/T_0$. In addition, the illumination phase ϕ of each individual trial was computed as[2] $\phi_u = \omega_0(T_{illum} - TZ_{-1})_{mod\,T_0}$, $\phi_l = \omega_0(T_{illum} - TH_{-1} + T_0/2)_{mod\,T_0}$, and the corresponding induced phase shift F was computed as $F_u = \omega_0(TZ_{+1} - TZ_{-1})_{mod\,T_0} - \pi$, $F_l = \omega_0(TH_{+1} - TH_{-1} + T_0/2)_{mod\,T_0} - \pi$.

We generated 2-D scatter plots for all trials with illumination phase as *x* coordinate and the corresponding phase shift as *y* coordinate. To visualize the distribution of the scatter points we generated bivariate histogram plots by grouping the data points into 2-D bins with 25 bins on both dimensions covering range $0{\sim}2\pi$ for *x* and range $-\pi{\sim}\pi$ for *y*, respectively. In addition, to indicate average tendency of phase shift depending on phase of illumination, we calculated a mean-curve representation of PRCs via a moving average operation. In this process, each mean was calculated over a sliding window of width 0.16π along the direction of ϕ from 0 to 2π. The 95% confidence interval relative to each window of data points was also computed and an integral number of them were displayed as filled area around the PRC curve. Through the computation, all statistical calculations followed the rules of directional statistics (10) since ϕ and F are circular variables defined in radians.

The Relaxation Oscillator Model for Locomotor Wave Generation

We first developed a relaxation oscillator model to simulate the rhythm generation during *C. elegans* locomotion. In this model, we incorporated a novel neuromuscular mechanism with a previously described biomechanical framework (7). Here, we only simulated the bending rhythms generated from the head region; the wave propagation dynamic is out of the scope of our study. Our phenomenological model does not contain detailed activities of individual neurons but focus on describing key neuromuscular mechanisms and their contributions to the rhythm generation.

First, to produce model variables that can be directly compared with experimental observations of moving animals, a biomechanical framework was first developed to describe worm's behavioral dynamics in its external environments. Following previous derivations for *C. elegans* biomechanics (7), the relationship between animal behavioral outputs and the active muscle moments can be described as follows:

---

[1] T_0 was computed as the average of differences of adjacent local maxima/minima before and after illumination; multiple cycles were used here to reduce noise. The validation of this calculation subjects to the assumption that a brief perturbation only affects one oscillatory cycle and the worm returns to normal oscillation in the next one.

[2] Here, phase of illumination and the corresponding phase shift were computed twice using zero (subscripted with u) and half-cycle (subscripted with l) phase points as references, respectively.

$$C_N \frac{\partial y}{\partial t} + a \frac{\partial^2 \kappa}{\partial s^2} + a_v \frac{\partial}{\partial t}\left(\frac{\partial^2 \kappa}{\partial s^2}\right) = m_a. \qquad \textbf{[S1]}$$

In Eq. S1, the first term indicates the external viscous force that is transverse to the body segment where C_N is the coefficient of viscous drag to the transverse movement and y denotes the lateral displacement of body segment; the second term indicates the internal elastic force where a is the bending modulus of the worm body; the third term indicates the internal viscous force where a_v is the coefficient of the body internal viscosity. On the right side of Eq. S1 is the active muscle moment m_a.

Taking the second partial derivative with respect to s on both sides of Eq. S1 and, under the small-amplitude approximation, using the linear relation, $\kappa \approx y_{ss}$, we arrive at:

$$C_N \frac{\partial \kappa}{\partial t} + a \frac{\partial^4 \kappa}{\partial s^4} + a_v \frac{\partial}{\partial t}\left(\frac{\partial^4 \kappa}{\partial s^4}\right) = \frac{\partial^2 m_a}{\partial s^2}. \qquad \textbf{[S2]}$$

For small-amplitude undulations, κ can be considered as a travelling sinusoidal wave with a small deviation, $\kappa(s,t) = \kappa_0 \sin(2\pi s/\lambda - \omega t) + \delta$, which leads to an approximation, $\kappa_{ssss} \approx (2\pi/\lambda)^4 \kappa$. Plugging this approximation into Eq. S2 while keeping s fixed, after some rearrangement, one gets:

$$\kappa + \frac{C_N \left(\frac{\lambda}{2\pi}\right)^4 + a_v}{a} \dot{\kappa} = \frac{\lambda^4}{(2\pi)^4 a} \frac{\partial^2 m_a}{\partial s^2}. \qquad \textbf{[S3]}$$

In terms of the dimensionless curvature $K = \kappa \cdot L$ and dimensionless muscle moment

$$M_a = \frac{\lambda^4 L}{(2\pi)^4 a} \frac{\partial^2 m_a}{\partial s^2}, \qquad \textbf{[S4]}$$

we can rewrite Eq. S3 as:

$$K + \tau_u \dot{K} = M_a\,, \qquad \textbf{[S5]}$$

where

$$\tau_u = \frac{C_N \left(\frac{\lambda}{2\pi}\right)^4 + a_v}{a}, \qquad \textbf{[S6]}$$

and we note that Eqs. S5 and S6 yield Eq. 1.

The above biomechanical framework in our model treats worm's body segment as a viscoelastic rod and describes how the body segment bends under the forces provided by the active muscle moment. However, the simulated oscillation in K comes from the rhythmicity of the active muscle moment which originates from the hypothesized neuromuscular mechanism described below (a relaxation-oscillation process):

i. Proprioceptive feedback is sensed as a linear combination of the current curvature value and the current rate of change of curvature, $P = K + b\dot{K}$ (black curve in Fig. 4D).
ii. During movement of bending, this proprioceptive feedback is constantly compared with two threshold values P_{th} and $-P_{th}$ (grey dashed bars in Fig. 4D).
iii. Once the feedback reaches either of the thresholds (the switch point as indicated by red circles in Fig. 4D), a switch command is initiated (blue square wave in Fig. 4E).

The switch command triggers the active muscle moment to change toward the opposite saturation value (black curve in Fig. 4E). To simulate the switch-triggered muscle transition we used a modified logistic function: $M_a(t) = \pm M_0 \cdot \tanh(t/2\tau_m)$. Here, the plus sign indicates the dorsal-to-ventral muscle moment transition while the minus sign indicates the opposite direction.

To initiate the oscillation in our model we set the system to bend toward the ventral side by setting $M_a|_{t=0} = M_0$ and $K|_{t=0} = 0$. During forward locomotion, the active muscle moment oscillates by undergoing a relaxation oscillation process: a relaxation subperiod during which M_a stays at a saturated bending state (M_0 for ventral bending, $-M_0$ for dorsal bending), alternating between a shorter subperiod during which M_a quickly transits toward the opposite state due to effects described in iii and iv. The bending curvature $K(t)$ which is driven by M_a in an exponential decaying manner (Eq. S5) follows the rhythmic activity of M_a, thereby also exhibiting an oscillatory dynamic (Fig. 4B).

This relaxation oscillator model reproduces two key features of free locomotion that we observed from experiments. First, freely moving worms exhibit nonsinusoidal curvature waveform with an intrinsic asymmetry: bending toward the ventral or dorsal directions occurs slower than straightening toward a straight posture during the locomotory cycle (Fig. 4F). Second, dynamic of the active muscle moment shows a trapezoidal waveform during forward locomotion (Fig. 2D *Inset* and Fig. 4E). These results are independent of external conditions but reflect intrinsic properties of the neuromuscular mechanisms underlying locomotion rhythm generation.

Note that parameters M_0, τ_u, and τ_m were estimated from data of free locomotion using phase portrait techniques described the following subsection. Parameters b and P_{th} were yet degenerate in this model of free locomotion. Here, we temporarily set $b = 0$ and then set P_{th} such that the oscillatory period predicted by model matched the average period measured from experiments with a minimum squared error:

$$P_{th} = \underset{P_{th}>0}{\operatorname{argmin}} \left(T_{model}(P_{th}) - T_{experiment}\right)^2. \qquad [\mathbf{S7}]$$

The nondegeneracy of b and P_{th} was determined by fitting the model to the experimental PRC as described in the later subsection so that the parameters for the model are provided as $M_0 = 8.45$, $\tau_u = 260\ ms$, $\tau_m = 50\ ms$, $b = 46\ ms$, and $P_{th} = 2.33$.

Measuring Bending Decay Time Scale and Amplitude of Active Muscle Moment

To estimate these two parameters, we applied a heuristic method that uses the shape properties of *C. elegans* free-running phase plot (Fig. 2D). From the curve in the figure, we noticed two 'flat' portions symmetrically distributed at quadrant *I* and *III* on the phase plane. Recalling Eq. 1 (or Eq. S5): $K + \tau_u \cdot \dot{K} = M_a(t)$, the two flat regions indicate that the scaled active muscle moment, $M_a(t)$, is nearly constant during the corresponding time bouts.

We then computed the linear correlation between variables K and $\dot{K}$ to identify the two 'flat' regions and, through linear fits, obtained two linear relations respectively: $\langle K\rangle + \tau_1 \cdot \langle\dot{K}\rangle = M_1$ (region 1) and $\langle K\rangle + \tau_2 \cdot \langle\dot{K}\rangle = M_2$ (region 2). Thus, the bending decay time scale τ_u and the amplitude of the scaled active muscle moment are estimated as $\widehat{\tau_u} = (\tau_1 + \tau_2)/2$ and $\widehat{M_0} = (|M_1| + |M_2|)/2$, respectively.

The above method used the phase plot measured from locomotion of worms swimming in a 17% dextran solution (120 mPa·s viscosity) as an example. However, it is also valid for estimating parameters of locomotion in other viscosities.

Measuring Active Moment Transition Time Scale

With τ_u (estimated from the above method), $\langle K\rangle$ and $\langle\dot{K}\rangle$ (measured from locomotion) plugged to the left side of Eq. 1, we were able to compute the waveform of the scaled active muscle moment $M_a(t)$ on the right side of Eq. 1. As expected and shown in Fig. 2D *Inset*, the curve of $M_a(t)$ is roughly centrally symmetric around point $(T_0/2, 0)$ on the plane, with two plateau portions indicating two saturated states for dorsal and ventral muscle contractions, respectively.

Between the two plateau portions indicates a period during which the active muscle moment is undergoing a ventral-to-dorsal (or vice-versa) transition. We used a modified logistic function to model the ventral-to-dorsal muscle moment transition (substituting t with $-t$ for transition in the other direction):

$$M_a(t) = M_0 \cdot \tanh\left(\frac{t}{2\tau_m}\right). \qquad [\mathbf{S8}]$$

To estimate τ_m, the exponential time constant for the transition of active muscle moment, we took the time derivative of Eq. S8 and took the absolute value of the resultant:

$$\left|\frac{dM_a}{dt}\right| = \frac{2M_0}{\tau_m} \cdot \frac{\exp(t/\tau_m)}{(1+\exp(t/\tau_m))^2}. \qquad [\mathbf{S9}]$$

We notice that when $t = 0$, the maximum of $|dM_a/dt|$ is achieved and the value is $M_0/2\tau_m$. On the other hand, the maximum of $|dM_a/dt|$ can be obtained from the experimental observation by simply finding the peak of $|dM_a/dt|$ curve where $M_a = \langle K(t)\rangle + \widehat{\tau_u} \cdot \langle dK(t)/dt\rangle$. Thus, τ_m can be estimated as:

$$\tau_m = \frac{M_0}{2} \cdot \left|\frac{dM_a}{dt}\right|_{max}^{-1}. \qquad [\mathbf{S10}]$$

Parameter Estimation

For our original threshold-switch model, parameters τ_u, τ_m, and M_0 were estimated from free locomotion experiments as described above. These three parameters nearly fully determine the biomechanical framework of *C. elegans* bending movements (governed by Eqs. S5 and S8). On the other hand, parameters b and P_{th} describe the proprioceptive feedback and the threshold-switch features in our model. Specifically, they characterize two threshold lines, $K + b\dot{K} = \pm P_{th}$ (as shown in Fig. 4C). The two switch points—defined by the intersection between the phase trajectory and the threshold lines on the phase plane—determine the timing of switches in the active muscle moment (see Fig. 4 C-E). We noted that the model behavioral output of free locomotion is degenerate with respect to these two parameters; the same outcome would be produced if the threshold lines cross the same pair of switch points. To first determine the free-moving dynamic as well as the switch points, we temporarily set $b = 0$ and then set P_{th} such that the oscillatory period defined by model matched the average period measured from the experiments.

To obtain the nondegeneracy of P_{th} and b, we fit our model to the experimental phase response curve using a global optimization procedure. Full procedure for the determination of b and P_{th} is given below.

Modeling Worm Oscillations in Varied Environments

When modeling worm oscillations in various environments, one should be aware that only parameters that are related to contact with external forces will change whereas parameters related to oscillator's internal properties will not. In terms of the endogenous parameters of our model, we used values that were previously determined, which are $\tau_m = 50\,ms$, $M_0 = 8.45$, $b = 46\,ms$, $P_{th} = 2.33$. For the exogenous parameters, we noted that the time constant of undulation, τ_u, is the only one such parameter that varies according to external conditions. According to Eq. S6, τ_u is explicitly determined in terms of other physical parameters, including biomechanical parameters measured in previous work (7): the internal viscosity of worm body is measured as $a_v = 5 \cdot 10^{-16} Nm^3 s$; the bending modulus of worm body is measured as $a = 9.5 \cdot 10^{-14} Nm^3$; $C_N = 31\eta$ is the coefficient of viscous drag to transverse movement (11), where η is the fluid viscosity. According to previous measurements of undulatory wavelengths in different viscous solutions (7), we applied a logarithm linear fit to the data points and set $\lambda = -0.158\log(\bar{\eta}) + 1.5$ for a continuous model realization in undulatory frequency and amplitude. Here, the dimensionless quantity $\bar{\eta}$ represents the value of viscosity in the unit $mPa \cdot s$.

Alternative Models for Locomotor Wave Generation

To further evaluate the performance of our original model, we explored three alternative models for simulating wave generation in order to make comparisons across these models and the experimental observations. Alternative models are based on three previously studied self-oscillator models described by 2-D nonlinear systems: the van der Pol, Rayleigh, and Stuart-Landau oscillators.

First, we developed a model oscillator in the form taken from the van der Pol Oscillator:

$$\ddot{K} + a_V(b_V K^2 - 1)\dot{K} + \omega_V^2 K = 0, \qquad [\mathbf{S11}]$$

where K indicates the nondimensional bending curvature. This model has a nonlinear damping term with a coefficient depending on K. Simulated oscillation is a limit cycle of the model (Fig. S7 A,D), given parameters $a_V = -0.026\,s^{-1}$, $b_V = -2.04$, $\omega_V = 5.51\,s^{-1}$.

Second, we developed a model oscillator by modifying the Rayleigh Oscillator:

$$\ddot{K} + a_R\left(b_R \dot{K}^2 - 1\right)\dot{K} + \omega_R^2 K = 0, \qquad [\mathbf{S12}]$$

where K again indicates the nondimensional bending curvature. This model has a nonlinear damping term with a coefficient depending on $\dot{K}$. Simulated oscillation is a limit cycle of the model (Fig. S7 B,E), given parameters $a_R = 2.73\,s^{-1}$, $b_R = 0.0023\,s^2$, $\omega_R = 5.6\,s^{-1}$.

Third, we developed a model oscillator by modifying the Stuart-Landau Oscillator:

$$\dot{Z} + \left(\frac{l}{2}|Z|^2 - \sigma\right)Z = 0. \qquad [\mathbf{S13}]$$

Here, the system is described in the complex domain where $Z = Z_r + iZ_i$, $l = l_r + il_i$ are complex variables, and σ is real. We let Z_r, the real part of Z, denote the nondimensional curvature K. This model has a nonlinear damping term with coefficient depending on $|Z|$. Simulated oscillation is a limit cycle of the model (Fig. S7 C,F), given parameters $l_r = 0.54\ s^{-1}$, $l_i = 0.52\ s^{-1}$, $\sigma = 5.54\ s^{-1}$.

The three alternative models produce free-running oscillatory dynamics with similar frequency and amplitude as measured from worms swimming in fluids with viscosity $120\ mPa \cdot s$.

Simulation of Optogenetic Inhibition

According to our experimental observations on the effect of the optogenetic muscle inhibition (Fig. 3 A,B), paralysis of muscles of the illuminated region initiated upon illumination (defined as $t = 0$ for Fig. 3B) and reached maximal effect approximately at $t = 0.3\ s$. Here, we modeled the process of muscle inhibition by multiplying the scaled active muscle moment, M_a, with a factor, $1 - Q(\Delta t)$, as a function of the time interval Δt in a bell-shaped form (Fig. S5, Eq. S14).

As described in our model, the dorsoventrally alternating feature of the active muscle moment during locomotion are described by the dynamics of $M_a(t)$. Specifically, $M_a(t)$ is positive when ventral muscles contract and dorsal muscles relax, and negative for the other half of the cycle. Therefore, in our threshold-switch model, specifically inhibiting dorsal- or ventral- or both-side muscles was computationally equivalent to conditionally modulating $M_a(t)$ with the bell-shaped modulating function depending on the sign of $M_a(t)$.

For simulating inhibition process in the three alternative models, we factored out a specific term from individual model equations as a generalized active muscle moment. We applied the bell-shaped modulating function to this term conditionally for each individual model. Detailed descriptions of implementing modeled inhibitions in alternative models are available from below.

To get a deeper understanding of how phase response curves are related to systems dynamics during wave generation, we systematically simulated transient muscle inhibitions on individual model oscillators at different times within a cycle period to generate model PRCs. To do that, we theoretically simulated the process of muscle inhibition by multiplying model active muscle moment with a modulatory factor, $1 - Q(\Delta t)$, which has a bell-shaped profile (Fig. S5):

$$Q(\Delta t) = \frac{H}{\left(1 + \left|\frac{\Delta t - r}{p}\right|^{2q}\right)}, \qquad [\mathbf{S14}]$$

where $r = 0.3\ s$ is the timing of the occurrence of maximal paralysis[3], H indicated the maximal degree of paralysis, and p, q measure the paralyzing rate and duration, respectively. To ensure sufficient smoothness during computation, we let $p = 0.3 \cdot 10^{-1/q}$ so that $Q|_{\Delta t=0} > 0.99$. Note that when modeling the dorsal-side-only muscle inhibition, the parameter H for describing max degree of optogenetic muscle inhibition was modulated to $H = 0.5 * H_{optimal}$ to qualitatively agree with experimental observations (Figs. 6 and S8). This factor accounts for unequal degrees of paralysis during ventral vs. dorsal illumination (Fig. S6), causing the PRC of dorsal-side illumination to show a relatively moderate response compared to ventral-side illumination.

To simulate the muscle inhibition on our threshold-switch model, we multiplied M_a with $(1 - Q)$ any time the model was to be inhibited during its oscillatory period. To apply this operation to the alternative models, we factored out a term as a generalized active muscle moment for each individual model and then multiplied it with the bell-shaped function described above. The generalized active muscle moment for the alternative models are implemented by modifying their original forms as follows:

a. For the van der Pol Oscillator, it is modified as:

$$\begin{cases} \ddot{K} + \left(-\widetilde{M_V} + P_V\right)\dot{K} + \omega_V^2 K = 0 \\ M_V = a_V(1 - b_V K^2) + P_V \end{cases} ; \qquad [\mathbf{S15}]$$

b. For the Rayleigh Oscillator, it is modified as:

[3] According to our experimental observations on the effect of muscle inhibition (Fig. 3 A,B), paralysis of muscles of the illuminated region initiated upon illumination (set as $t = 0$) and reached maximal effect approximately at $t = 0.3\ s$.

$$\begin{cases} \ddot{K} + \left(-\widetilde{M_R} + P_R\right)\dot{K} + \omega_R^2 K = 0 \\ M_R = a_R\left(1 - b_R\dot{K}^2\right) + P_R \end{cases} ; \qquad [\mathbf{S16}]$$

c. For the Stuart-Landau Oscillator, it is modified as:

$$\begin{cases} \dot{Z} + \left(-\widetilde{M_S} + P_S\right)Z = 0 \\ M_S = \sigma - \frac{l}{2}|Z|^2 + P_S \end{cases} . \qquad [\mathbf{S17}]$$

For each individual model listed above, $\widetilde{M_i}$ (subscript i represents V, R, and S, respectively) is the generalized muscle moment which is to be multiplied by the bell-shaped factor $(1 - Q)$ upon perturbation, and P_i is the additional damping coefficient. Note that the minus sign prior to M_i in the first equation of each set indicates that M_i is a negative damping term that provides power to the system, while P_i is set positive for modeling the effect of bending toward the straight posture due to internal and external viscosity. Also note that Eqs. S15-17 would be equivalent to their original form (Eqs. S11-13) when inhibition is absent (in this case, $\widetilde{M_i} = M_i$).

By modeling the muscle inhibition process during locomotion, we were able to perform simulations of phase response experiments on individual models to produce perturbed systems dynamics (Fig. S7 G-I) and the corresponding PRCs (Fig. S7 J-L and Fig. S8).

Optimization of Models

For each individual model we developed, parameters were determined via a two-round fitting process. First, a subset of parameters was determined by fitting the model to observations of free-moving dynamics; the model could generate free-moving dynamics close to observations at this point. Second, the rest of the parameters were settled by fitting it to experimental phase response curves; a model would be fully determined at this point. Detailed descriptions of the two-step optimization procedure for individual models are provided as follows:

For the original threshold-switch model, parameters τ_u, M_0, and τ_m were explicitly estimated from the experiments of free locomotion using phase portrait techniques described above. To simulate free locomotion, we further determined the position of switch points in the model (as indicated in Fig. 4C red circle), which we did using method described by Eq. S7. Next, we plugged the determined parameters into the model and conducted the second round of optimization by fitting the model with undetermined parameters P_{th}, b, as well as the parameters for simulating muscle inhibition—H and q. We generated model PRC by perturbing the model oscillator at different times within a cycle period and settled the parameters such that the model PRC matched the experimental one with a minimum mean squared error (MSE)[4]:

$$(P_{th}, b, H, q) = \underset{P_{th},b,H,q}{\operatorname{argmin}} \sum_0^{2\pi} \left(PRC_{model}(P_{th}, b, H, q; \phi) - PRC_{experiment}(\phi)\right)^2 \Delta\phi \qquad [\mathbf{S18}]$$

To find the parameters that minimize the difference, a global minimum search was performed using the MATLAB function 'GlobalSearch' (12). When run, the function repeatedly uses a local minimum solver with different batches of parameter range and attempts to locate a solution that produces the lowest MSE value.

Similarly, the two-step optimization procedures for individual alternative models are summarized in Table S1.

References for Supplemental Information

1. B. A. Bamber, A. A. Beg, R. E. Twyman, E. M. Jorgensen, The Caenorhabditis elegans unc-49 locus encodes multiple subunits of a heteromultimeric GABA receptor. *Journal of Neuroscience* **19**, 5348–5359 (1999).

[4] During the computation of MSE, values of both model and experimental PRCs were sampled across the entire range of ϕ with 100 evenly distributed samples. In this case, $\Delta\phi = 2\pi/100$.

2. B. Van der Pol, LXXXVIII. On “relaxation-oscillations.” *The London, Edinburgh, and Dublin Philosophical Magazine and Journal of Science* **2**, 978–992 (1926).

3. R. FitzHugh, Impulses and physiological states in theoretical models of nerve membrane. *Biophysical journal* **1**, 445 (1961).

4. J. Nagumo, S. Arimoto, S. Yoshizawa, An active pulse transmission line simulating nerve axon. *Proceedings of the IRE* **50**, 2061–2070 (1962).

5. J. W. S. B. Rayleigh, *The theory of sound* (Macmillan, 1896).

6. J. A. Acebrón, L. L. Bonilla, C. J. P. Vicente, F. Ritort, R. Spigler, The Kuramoto model: A simple paradigm for synchronization phenomena. *Reviews of modern physics* **77**, 137 (2005).

7. C. Fang-Yen, *et al.*, Biomechanical analysis of gait adaptation in the nematode Caenorhabditis elegans. *Proceedings of the National Academy of Sciences* **107**, 20323–20328 (2010).

8. T. Stiernagle, *Maintenance of C. elegans (February 11, 2006), WormBook, ed. The C. elegans Research Community, WormBook, doi/10.1895/wormbook. 1.101. 1* (2006).

9. A. D. Fouad, *et al.*, Distributed rhythm generators underlie Caenorhabditis elegans forward locomotion. *Elife* **7**, e29913 (2018).

10. N. I. Fisher, T. Lewis, B. J. Embleton, *Statistical analysis of spherical data* (Cambridge university press, 1993).

11. D. F. Katz, J. R. Blake, S. L. Paveri-Fontana, On the movement of slender bodies near plane boundaries at low Reynolds number. *Journal of Fluid Mechanics* **72**, 529–540 (1975).

12. Z. Ugray, *et al.*, Scatter search and local NLP solvers: A multistart framework for global optimization. *INFORMS Journal on Computing* **19**, 328–340 (2007).

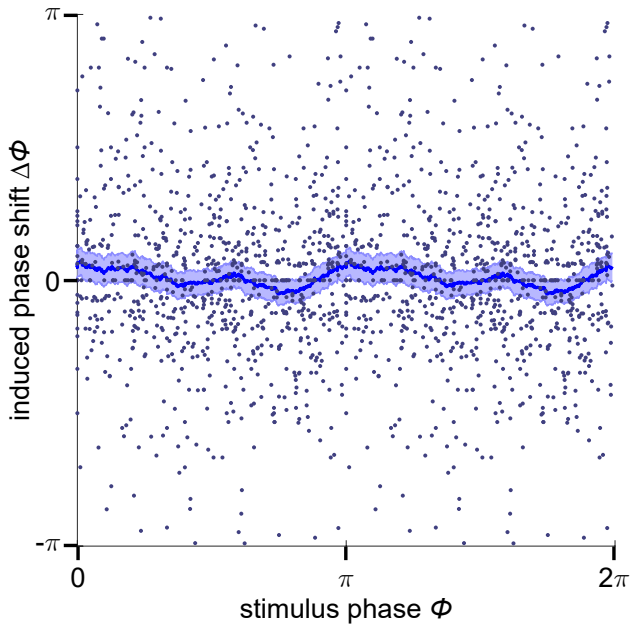

Figure S1. Phase response curve of *Pmyo-3::NpHR* worms (ATR- control group, 414 trials using 116 worms). Each point represents a single illumination (0.1 s duration, 532 nm wavelength) of one worm. Filled area represents 95% confidence interval.

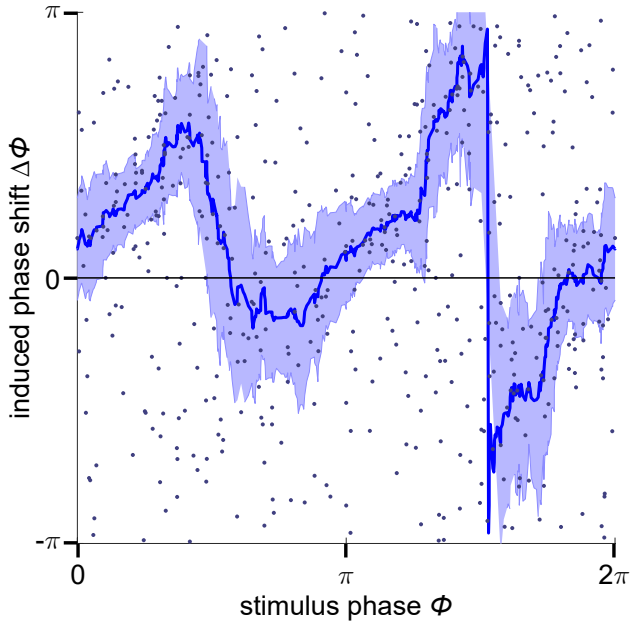

Figure S2. Phase response curve of YX119, transgenic worms that express *NpHR* in the body wall muscles but lack the GABA receptor for the D-type motor neurons. Curve was obtained from 259 trials of transient inhibitions of head muscles using 192 worms. Each point represents a single illumination (0.1 s duration, 532 nm wavelength) of one worm. Filled area represents 95% confidence interval.

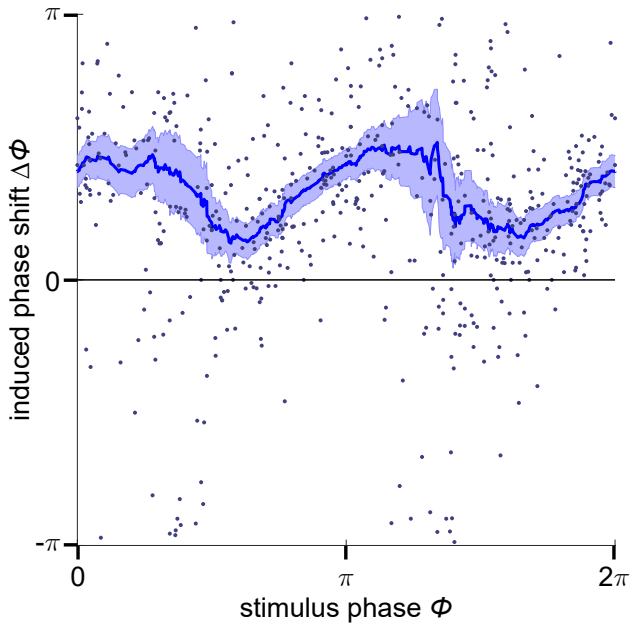

Figure S3. Phase response curve of YX205, transgenic worms that express *NpHR* in all cholinergic neurons (*Punc-17::NpHR::ECFP*). Curve was obtained from 270 trials of transient inhibitions of cholinergic neurons in the head region using 135 worms. Each point represents a single illumination (0.055 s duration, 532 nm wavelength) of one worm. Filled area represents 95% confidence interval.

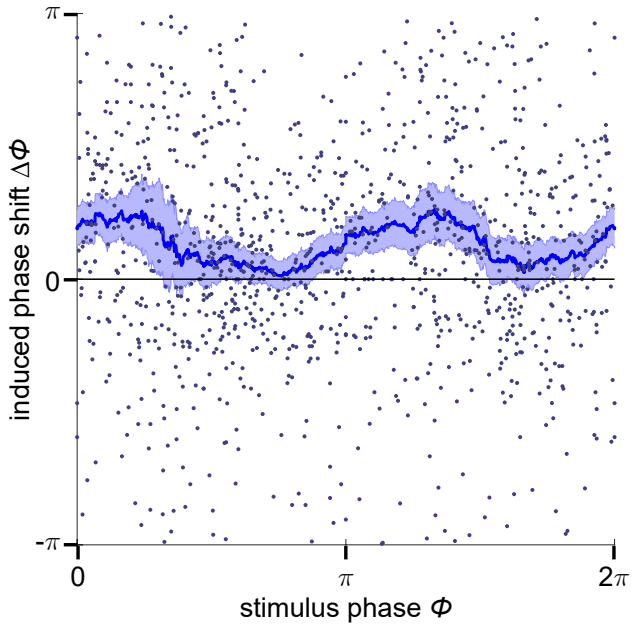

Figure S4. Phase response curve of WEN01, transgenic worms that express Arch in the B-type motor neurons (*Pacr-5::Arch-mCherry*). Curve was obtained from 551 trials of transient inhibitions of the B-type motor neurons in the head region using 160 worms. Each point represents a single illumination (0.055 s duration, 532 nm wavelength) of one worm. Filled area represents 95% confidence interval.

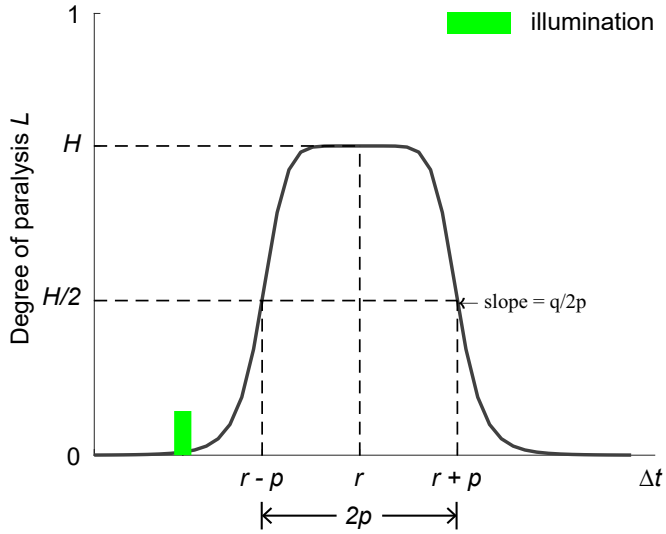

Figure S5. Bell-shaped function for modeling the optogenetic muscle inhibition (Eq. S14). The curve models the degree of paralysis due to the optogenetic muscle inhibition as a function of time. Referring to Eq. S14, the fractional variable H describes the reduced proportion of muscle moment when a worm reaches maximal paralysis after illumination. r describes the time of maximal paralysis with respect to the occurrence of illumination. p determines the time interval during which the paralyzing degree exceeds $H/2$. q and p together determine the paralyzing rate.

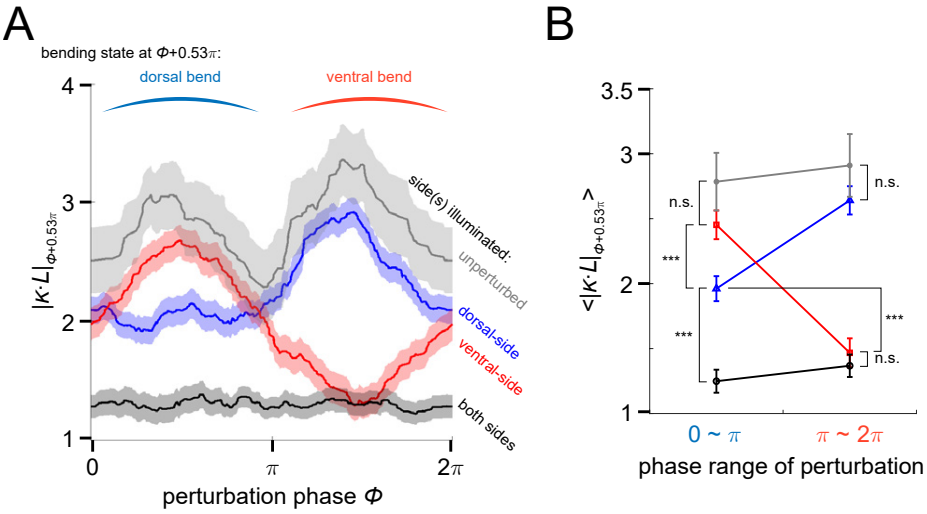

Figure S6. Paralyzing effect analysis of muscle inhibitions induced by illumination on different sides of worm's head segment. (A) Spectra of paralyzing effects across all phases of illuminations, represented by absolute curvature $|K|$ of the head region. $|K|$ shown on *y*-axis is the value obtained 0.53π later in phase (or 0.3 s in time with respect to locomotion period 1.13 s) after the illumination phase ϕ. The specific phase difference 0.53π (or 0.3 s time difference) was chosen for computing the paralyzing effects because max paralysis is achieved at ~0.3 s after illumination as shown in Fig. 3B. Grey curve represents control ATR+ (no light) group (414 trials using 116 worms). Red curve represents ATR+ group with only ventral side being illuminated (373 trials using 176 worms). Blue curve represents ATR+ group with only dorsal side being illuminated (576 trials using 242 worms). Black curve represents ATR+ group with both sides being illuminated (991 trials using 337 worms). All curves were obtained using a moving average along the *x*-axis with 0.4π in bin width and filled areas represent 95% confidence interval. (B) Average paralyzing effects during dorsal bend and ventral bend, represented by mean absolute curvature $\langle|K|\rangle$ averaged across range $[0,\pi]$ (dorsal bend) and $[\pi,2\pi]$ (ventral bend), respectively. Colors indicate different conditions of experiment in the same way as in A. (***) indicates p<0.0005 using paired *t* test.

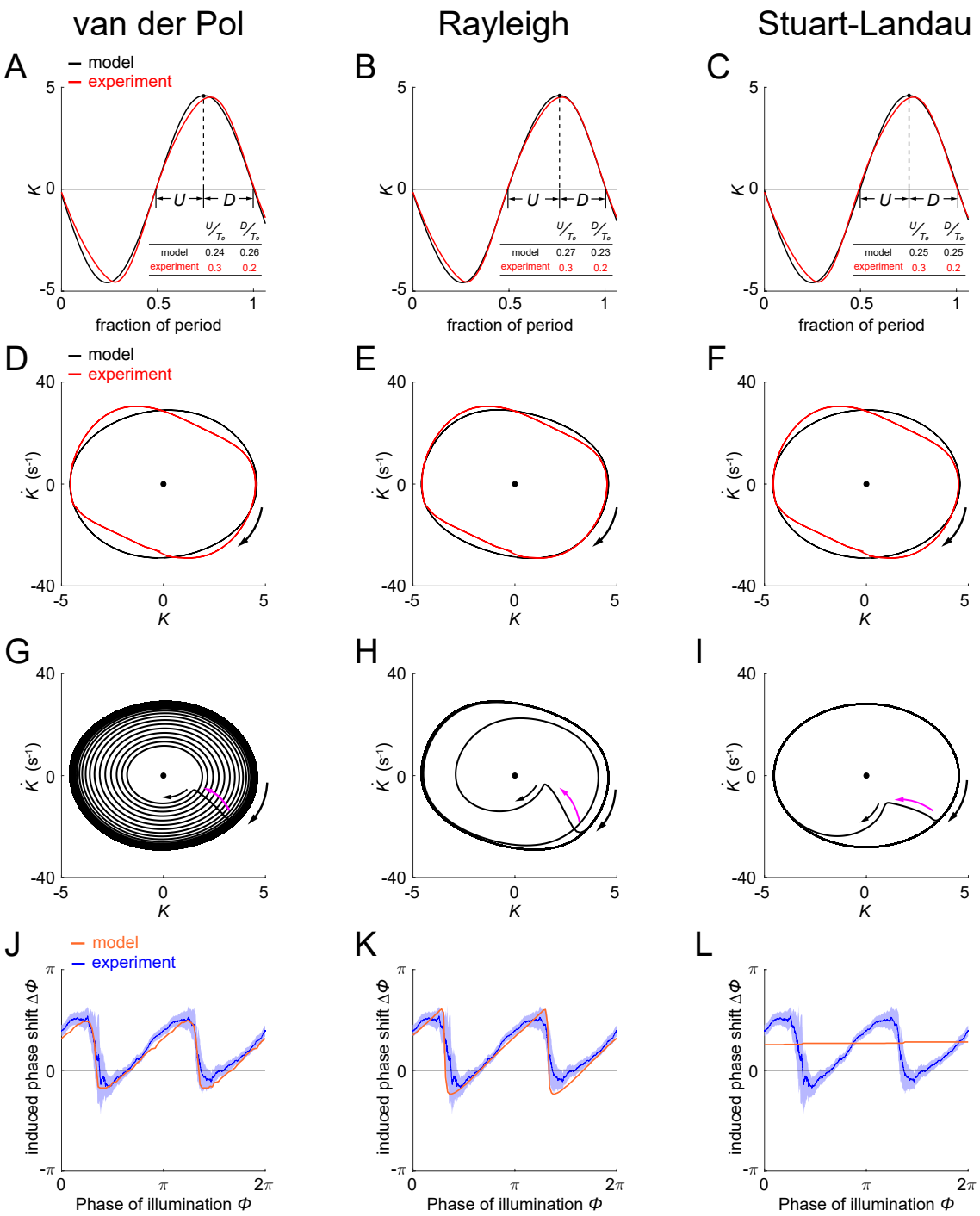

Figure S7. Performance of alternative models: van der Pol oscillator (column 1), Rayleigh oscillator (column 2), and Stuart-Landau oscillator (column 3). (A-C) Time varying curvature of worm's head region, measured by experiment (red, 5047 cycles using 116 worms) and model (black). Three models match experimental curvature with MSEs ≈ 0.44, 0.18, and 0.39, respectively. (Inset table) U/T_0 (fraction of period of bending toward the ventral or dorsal directions) and D/T_0 (fraction of period of straightening toward a straight posture), for experiments or models. (D-F) Phase portrait graphs of the free-running dynamics shown in A-C, from experiments (red) and models (black). Arrow indicates clockwise movement. (G-I) Phase plots showing each model perturbed (indicated by purple arrow) away from stable limit cycle and then recovering toward

equilibrium. (J-K) Phase response curves with respect to both-side muscle inhibition, from experiments (blue, 991 trials using 337 worms) and models (orange). Three models match experimental PRC with MSEs ≈ 0.21, 0.37, and 0.72, respectively.

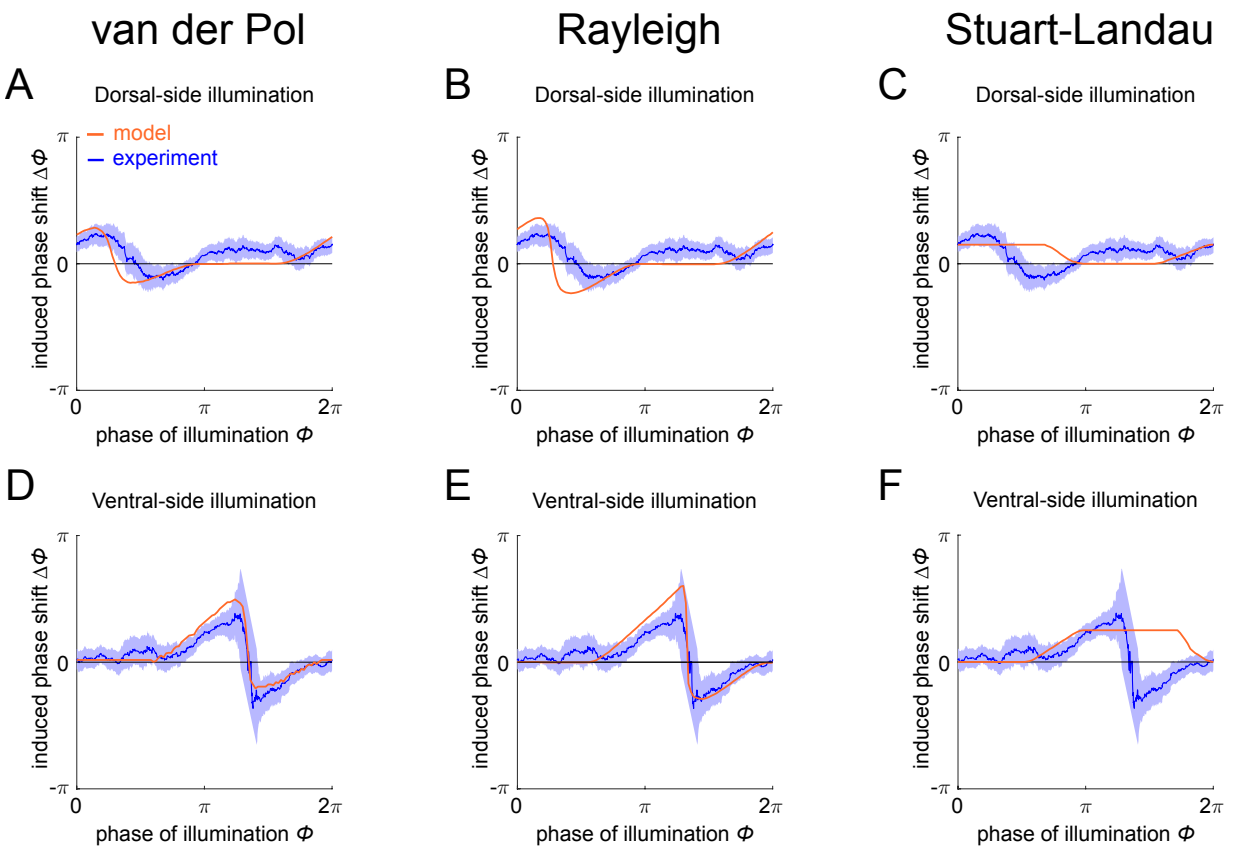

Figure S8. Phase response curves with respect to single-side muscle inhibition, simulated from alternative models: van der Pol oscillator (column 1), Rayleigh oscillator (column 2), and Stuart-Landau oscillator (column 3). (A-C) PRCs with respect to dorsal-side muscle inhibition, from experiments (blue, 576 trials using 242 worms) and models (orange). (D-F) PRCs with respect to ventral-side muscle inhibition, from experiments (blue, 373 trials using 176 worms) and models (orange). Filled areas of all experimental PRCs represent 95% confidence interval with respect to each bin of data points.

Table S1. Objective functions used in the optimization procedures for alternative models

Type	Free locomotion model	Complete model
van der Pol	$\underset{a_V,b_V,\omega_V}{\operatorname{argmin}}\left(\left(\frac{T_{vdP}}{T_{expt}}-1\right)^2+\left(\frac{A_{vdP}}{A_{exp}}-1\right)^2\right)$	$\underset{p_V,H,q}{\operatorname{argmin}}\sum_0^{2\pi}\left(PRC_{vdP}(\phi)-PRC_{exp}(\phi)\right)^2\Delta\phi$
Rayleigh	$\underset{a_R,b_R,\omega_R}{\operatorname{argmin}}\left(\left(\frac{T_{Rayleigh}}{T_{expt}}-1\right)^2+\left(\frac{A_{Rayleigh}}{A_{exp}}-1\right)^2\right)$	$\underset{p_R,H,q}{\operatorname{argmin}}\sum_0^{2\pi}\left(PRC_{Rayleigh}(\phi)-PRC_{exp}(\phi)\right)^2\Delta\phi$
Stuart-Landau	$\underset{a_S,b_S,\omega_S}{\operatorname{argmin}}\left(\left(\frac{T_{SL}}{T_{expt}}-1\right)^2+\left(\frac{A_{SL}}{A_{exp}}-1\right)^2\right)$	$\underset{p_S,H,q}{\operatorname{argmin}}\sum_0^{2\pi}\left(PRC_{SL}(\phi)-PRC_{exp}(\phi)\right)^2\Delta\phi$

Two-step optimization procedure for van der Pol, Rayleigh, and Stuart-Landau oscillators. The first-step optimization determines part of parameters such that individual models generate free locomotion dynamics. The second-step optimization leads to complete models such that models' perturbed dynamics and phase response curves are produced.

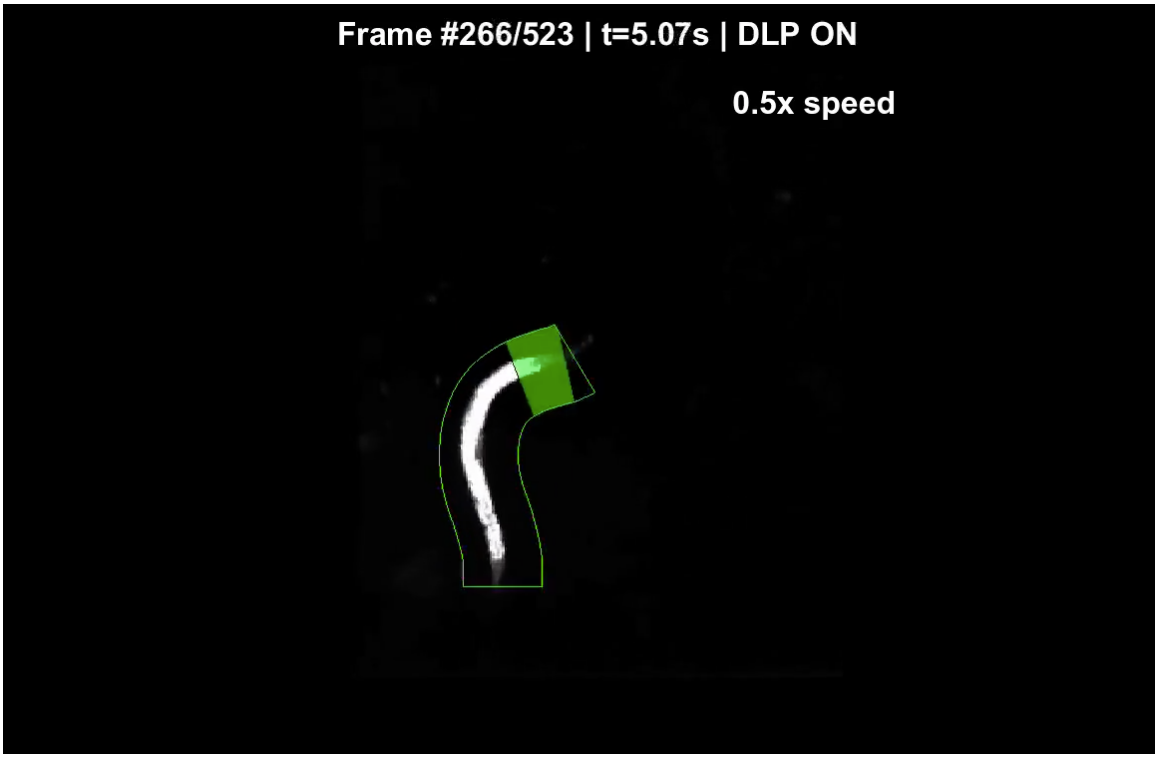

Supplemental Video S1. Transient illumination of the anterior region of a freely moving *Pmyo-3::NpHR* worm. Solid green region indicates timing and location of illumination.